Progress and Trends in Non-destructive Testing for Thermal Barrier Coatings Based on Infrared Thermography: A Review

Jianguo Zhu[1,2] · Zhuangzhuang Mao[2] · Dongliang Wu[3] · Jiangfan Zhou[4] · Dacheng Jiao[2] · Wenxiong Shi[5] · Wenying Zhu[2] · Zhanwei Liu[2]

Abstract

Thermal barrier coatings (TBCs), as effective thermal protection separating the substrate from high-temperature combustion gases and reducing the substrate temperature, are widely used in aerospace and other fields. During the service cycle of life, surface crack defects, interface disbond defects, and coating thickness changes are the main non-destructive testing (NDT) objects of TBCs. In this paper, the main active infrared thermography NDT techniques including the optical infrared thermography testing, the ultrasonic infrared thermography testing, and the microwave thermography testing techniques are reviewed. Through the summary and highlight of the detection principle and application status of these state-of-the-art techniques, the development of the active infrared thermography DNT technique in TBCs is presented. By comparing the sensitivity, advantages, and disadvantages of the techniques in TBC NDT, can provide a significant reference for researchers to choose an appropriate method. It is noteworthy that fabrication techniques of artificial defects for calibration of the active infrared thermography NDT technique inspection of TBC systems are also reviewed. Moreover, future trends in NDT for the TBC system based on the active infrared thermography NDT technique are also discussed and analyzed.

Keywords Non-destructive testing · Thermal barrier coatings · Optical infrared thermography · Ultrasonic infrared thermography · Microwave thermography

1 Introduction

In recent decades, with the development of many high-end industrial technologies, the performance of aero-engines, which has the reputation of "the jewel in the crown", has also been continuously improved [1, 2]. However, as aero-engines become more advanced, the temperature and

Jianguo Zhu and Zhuangzhuang Mao are co-first authors.
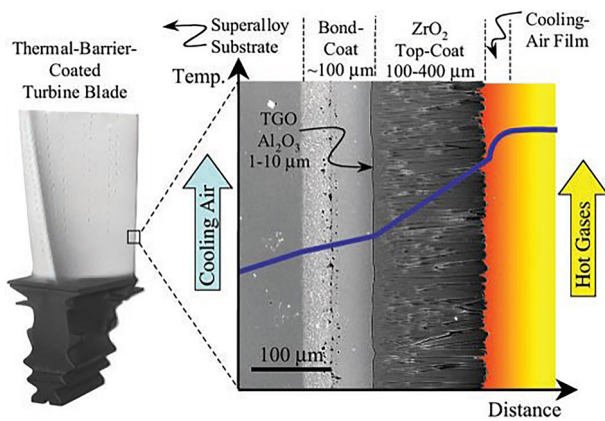
✉ Zhanwei Liu
liuzw@bit.edu.cn

1 Department of Mechanics and Engineering Science, Jiangsu University, Jiangsu 212013, China

2 School of Aerospace Engineering, Beijing Institute of Technology, Beijing 100081, China

3 Beijing Institute of Spacecraft Environment Engineering, Beijing 100020, China

4 Beijing Institute of Structure & Environment Engineering, Beijing 100076, China

5 AML, Department of Engineering Mechanics, Tsinghua University, Beijing 100084, China

pressure required for the turbine blades to operate in the combustion chamber with a high temperature plume increases. Although the turbine blade is made of high temperature resistant materials and adopts cooling gas film technology, there is still a 100–400 °C temperature gap between the extreme temperature it can withstand and the ambient temperature inside the combustion chamber. In response to this situation, the TBC technique, coating a certain thickness and durability of insulating ceramic film on the surface of turbine blades through atmospheric plasma spraying (APS), electron beam physical vapor deposition (EB-PVD), or other methods [3, 4], come into being. TBCs separate the turbine blade from the high temperature plume and achieves the purposes of reducing the temperature of the turbine blade, providing further thermal protection for the blade base material, and improving the efficiency of the aero-engine. Figure 1 is a schematic diagram of a turbine blade coated with TBCs [5]. The TBC is generally composed of three layers of materials: super-alloy substrate, bond coating, and ceramic coating. The super-alloy substrate provides structural support for TBCs. The ceramic

Fig. 1 Schematic diagram of turbine blade coated with TBCs [5]

Fig. 2 Surface crack defects and interface disbond defects

coating has the function of thermal barrier and erosion resistance. The middle bond coating connects the ceramic coating and the super-alloy substrate and improves the oxidation resistance of the super-alloy substrate. The TBC not only enables turbine blades to operate at high temperatures that they could not bear but also enables them to have high fracture toughness, impact resistance, and high-speed friction performance. Therefore, the TBC has also been applied to marine propulsion, nuclear reactor, and many other industrial fields [6–8].

Surface cracks in ceramic coating and interface cracks along the thermally grown oxide (TGO) interface are the two main failure modes in TBCs [9, 10]. Furthermore, the TBC is a multi-layer structure system, and each layer has different physical, thermal, and mechanical properties. The complex structure and harsh service environment of TBCs cause complicated stress distribution inside the coating and at the interface position under the combined action of heat, force, and chemistry. If the superimposed stress exceeds the critical value that the coating or the interface can withstand, cracks will occur and expand inside the coating [11, 12]. Besides, a deep surface crack with a certain width may form a passage for high temperature and oxygen, which accelerates the generation and extension of interface crack and eventually makes TBCs off from the substrate in advance [13, 14]. Therefore, as shown in Fig. 2, the TBC is prone to surface crack defects and interface disbond defects. As the defects in the TBC evolve, it can lead to premature failure of turbine blades and even catastrophic consequences. The uniqueness of TBC's defect characteristics makes traditional NDT, such as acoustic emission, penetration testing, eddy current testing, ultrasonic testing, and ray testing [15–23], have limitations in technology and testing efficiency. Therefore, it is of great significance to develop novel NDT techniques for TBCs defects.

The coating thickness of TBCs is not only a parameter of the geometrical property of the coatings themselves, but also an important indicator for evaluating the coatings' quality, performance, and service life [24]. However, the thinning and peeling-off of TBC could be found due to the effect of harsh operating conditions, including erosion, corrosion, and foreign object damage [25–27]. The loss in TBC thickness poses a severe threat to the structural integrity of aero-engine blade, causing the aero-engine failure and accidents. Therefore, it is imperative to periodically and non-destructively evaluate the thickness of TBC of the in-service aero-engine blade [28].
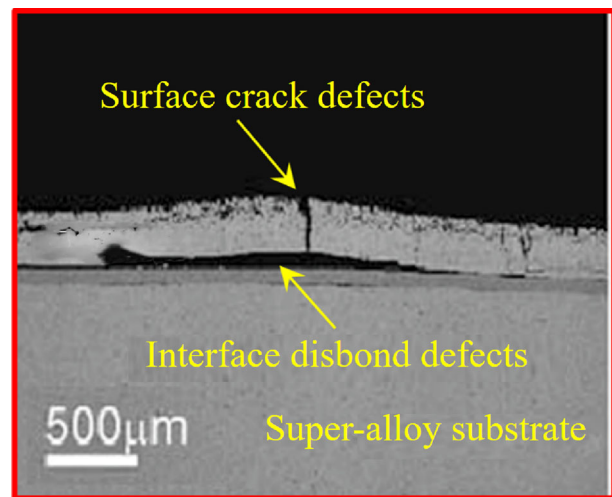
Therefore, the NDT of TBC mainly focuses on surface crack defects, interface disbond defects, and the coating thickness changes.

2 Advanced Infrared Thermography NDT Techniques

The active infrared thermography technique [29–31], as a burgeoning and advanced NDT technique, has been widely researched and applied in recent years. Under certain circumstances, surface defects, internal defects or coating thickness changes of the specimen will cause the surface temperature to change. By measuring and post-processing, the thermal response signal on the surface of the specimen, surface defects, internal defects, or coating thickness changes can be detected non-destructively. The thermal response signal on the surface of the specimen can be radiated by self-heating or thermal excitation. Therefore, the active infrared thermography NDT technique has the advantages of a large detection area, intuitive detection results, fast detection speed, non-contact detection, and simple operation.

2.1 Theoretical Basis of Active Infrared Thermography NDT Technique

The active infrared thermography NDT technique uses the corresponding relationship between thermal radiation and temperature. With different forms of active thermal excitation, the heteromorphic structure of the object can be represented by the difference in the surface temperature distribution, and then the defects or coating thickness can be accurately evaluated. The heat flow is associated with measurable temperature scales, but it cannot be measured directly. Therefore, once the temperature distribution $T(r, t)$ in an object is determined, the heat flow can be calculated using a law connecting heat flow with temperature, or Fourier's law [32]

$$q(r, t) = -\lambda \nabla T(r, t) \tag{1}$$

where $q(r, t)$ represents the heat flux per unit time on the unit isothermal surface in the direction of temperature reduction, λ is the thermal conductivity of the material, and $\nabla T(r, t)$ is the temperature gradient.

Fourier's law shows the relationship between heat flux and the temperature gradient, and it is useful for both steady and unsteady fields [33]. Then, the differential equation of heat conduction used to describe the internal relationship of the temperature field in the time–space domain is

$$\nabla^2 T(r, t) + \frac{q_v}{\lambda} = \frac{1}{\alpha} \frac{\partial T(r, t)}{\partial t} \tag{2}$$

where $\alpha = \lambda/\rho c$ is the thermal diffusivity, and q_v denotes the term of the heat source. From this, the theoretical model of infrared thermography NDT can be analyzed by combining this equation with the boundary conditions.

In terms of radiation, the total radiation intensity of a gray body is equal to the total radiation intensity of a blackbody, multiplied by the emission coefficient of the gray body; that is, the radiation of a gray body satisfies Stephen-Boltzmann law [34, 35]

$$W = \varepsilon \sigma T^4 \tag{3}$$

where ε is the emission coefficient of the gray body, σ is the Stephen–Boltzmann constant, W and T are the radiation intensity and absolute temperature of the object, respectively.

When the thermal signal is applied to the surface of the object, if the material is uniform and has no defects or coating thickness changes in its propagation direction, the thermal wave will propagate smoothly in the body. Finally, the thermal response signal accumulated on the surface is uniformly distributed, that is, the temperature distribution on the surface of the specimen is the same, and there is no abnormality. If there are defects in the specimen, the reflection will occur when the heatwave propagates to the defect, resulting in the sudden change of surface temperature distribution [36]. If there are coating thickness changes in the specimen, the change will also occur with the surface temperature distribution.

2.2 Classification of Active Infrared Thermography NDT Technique

According to the different thermal excitation properties, this paper divides the active infrared thermography NDT technique into the optical infrared thermography testing [37–43], the ultrasonic infrared thermography testing [44–46], and the microwave thermography testing [47–54]. As shown in Fig. 3, the three testing techniques are further classified according to the characteristics of application objects of the excitation, and all the corresponding principles are analyzed theoretically.

2.2.1 Optical Infrared Thermography Testing

The optical infrared thermography testing is an NDT technique with optical waves as the excitation source. According to the characteristics of thermal excitation, the optical infrared thermography testing can be classified into the optical pulsed thermography testing, the optical lock-in thermography testing, the structural optical scanning thermography testing, and the non-stationary thermal wave imaging testing.

Theoretical Basis of Optical Pulsed Thermography Testing

As shown in Fig. 4, the optical pulsed thermography testing is usually applied to the specimen with internal defects. When a pulsed heat source is irradiated to the surface of the specimen (Fig. 4a), the abrupt change will appear in the thermal response signal collected by the infrared camera (Fig. 4b). Therefore, the surface of the specimen satisfies the one-dimensional heat conduction equation

$$\frac{\partial^2 T(z, t)}{\partial z^2} - \frac{\rho c}{\lambda} \frac{\partial T(z, t)}{\partial t} = -\frac{q_0 \delta(t)}{\lambda} \tag{4}$$

where q_0 is the heating intensity, which refers to the power of the heat source, $\delta(t)$ is the unit pulse function, z is the direction of heat flow injection and propagation, λ is thermal conductivity, ρ is the density, c is the specific heat, T is the temperature, and t is the time.

Assuming that the specimen is a semi-infinite space, the temperature of the specimen is then obtained by solving the equation [36]

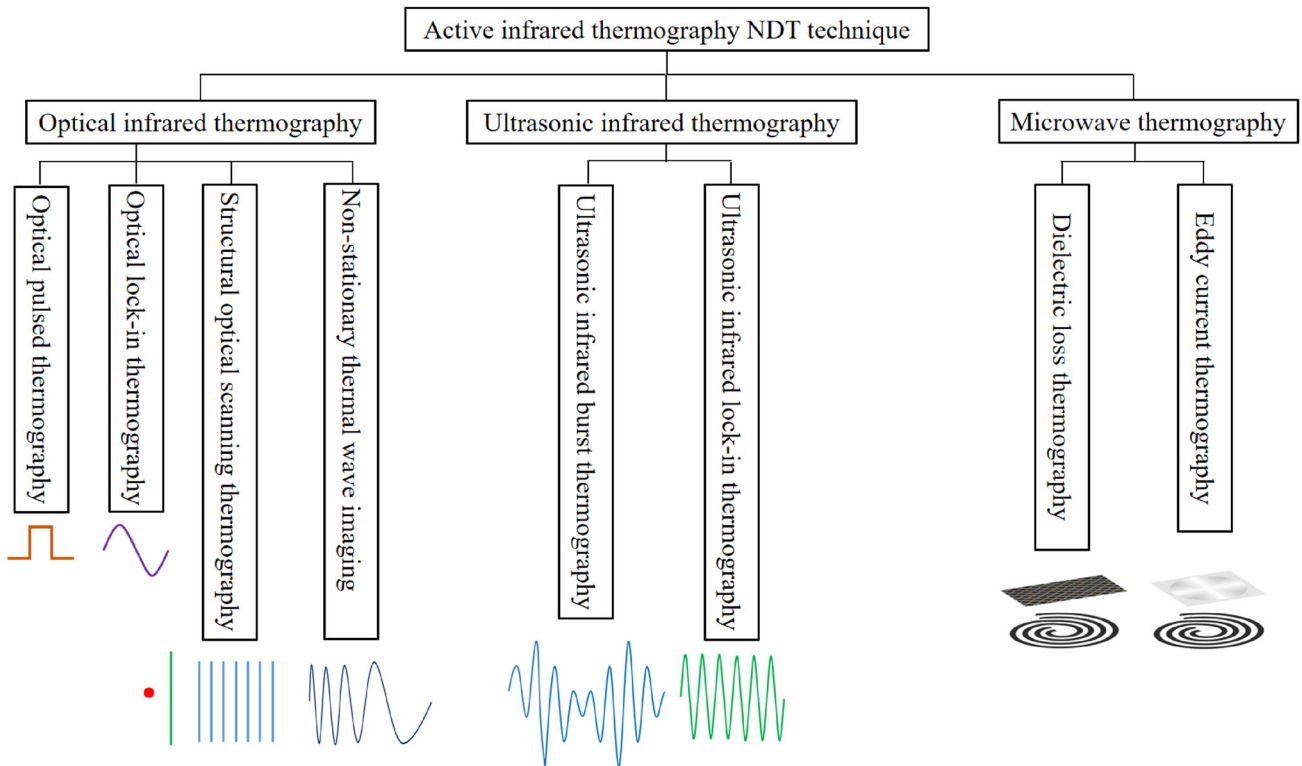$$T_n(z, t) = \frac{q_0}{\sqrt{\pi \rho c \lambda t}} \exp\left(-\frac{z^2}{4\alpha t}\right) \tag{5}$$

Fig. 3 Main testing technique of active infrared thermography
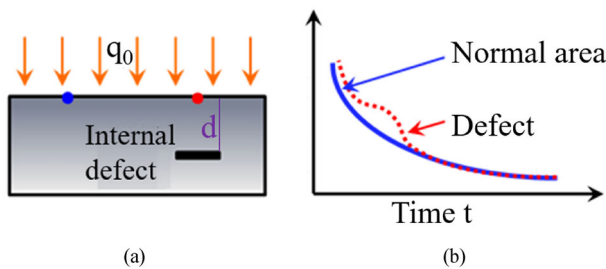

(a)   (b)

Fig. 4 Schematic diagram of optical pulsed thermography testing. **a** Specimen with defects irradiated by pulsed heat source. **b** Thermal response signal collected by infrared camera

where α is the thermal diffusion coefficient. When the thermal wave propagates to the defect at a depth d from the surface, it will be stopped and reflected. Then, the corresponding surface temperature of the defect area is found by

$$T_d(0, t) = \frac{q_0}{\sqrt{\pi \rho c \lambda t}} \left[1 + 2 \exp(-\frac{d^2}{\alpha t}) \right] \qquad (6)$$

It should be noted that the Eq. 6 is the approximation of the slab solution at the first term of the infinite summation. Besides, the main application of Eq. (6) is that the depth of the defect is a very small number for the thickness of the specimen [55]. Finally, the surface temperature difference is

obtained using the equation

$$\Delta T = T_d(0, t) - T_n(0, t) = \frac{2q_0}{\sqrt{\pi \rho c \lambda t}} \exp\left(-\frac{d^2}{\alpha t}\right) \qquad (7)$$

Therefore, after the pulse heating, the defect depth can be determined based on time. This corresponds to the peak temperature difference in the equation

$$t_{\max} = \frac{2d^2}{\alpha} \qquad (8)$$

Due to the short-acting time of the optical pulsed thermography testing, it can be used for transient measurement, so it has a wide range of application prospects. Although the optical pulsed thermography testing is simple and practical, it also has shortcomings. For example, this technique works well for defect detection in flat panel components but has difficulty with complex structural components. Moreover, it is limited by the thicknesses of the specimen to be inspected. When the specimen thickness is large, this technique is difficult to detect defects. In addition, this technique usually requires high uniformity of the pulsed heat source.

Theoretical Basis of Optical Lock-In Thermography Testing

The optical lock-in thermography testing uses the periodic modulated thermal excitation to heat the specimen, and it

is usually applied to specimens with internal defects. The temperature change caused on the surface of the specimen will produce a difference in amplitude and phase compared with the defect-free area, and then defects information inside the specimen can be analyzed.

Assuming that the specimen is an isotropic slab material and its plane area is much larger than its thickness, the longitudinal diffusion process of the thermal wave in the specimen satisfies the one-dimensional heat conduction constitutive equation shown in Eq. (4). The heat flow intensity of the thermal excitation of the optical lock-in thermography testing is a sine or cosine function that changes with time, and it can be calculated by the equation

$$q = \frac{Q}{2}[1 + \cos(2\pi f_e t)] = q_{tem} + q_{osc} \qquad (9)$$

where Q is the peak value of the heat flow intensity, f_e is the modulation frequency of the thermal excitation, q_{tem} is the direct current part of the heat flow intensity, q_{osc} is the alternating current part of the heat flow intensity.

The direct current part of the heat flow function makes the surface temperature of the specimen continue to rise, but the temperature also changes periodically under the influence of the alternating current part, and its frequency is consistent with the modulation frequency of the thermal excitation. As time goes by, the heat exchange at various points inside the specimen gradually reaches equilibrium. At this time, the surface temperature changes periodically, which means that the temperature change is in a steady state process. The initial temperature is

$$T(z, t)|_{t=0} = T_\infty \qquad (10)$$

The boundary condition of the upper surface of the specimen is

$$-\lambda \frac{\partial T(z, t)}{\partial z}\bigg|_{z=0} = q - h[T(0, t) - T_\infty] \qquad (11)$$

The boundary condition of the lower surface of the specimen is

$$-\lambda \frac{\partial T(z, t)}{\partial z}\bigg|_{z=L} = h[T(L, t) - T_\infty] \qquad (12)$$

where T_∞ is the ambient temperature, h is the heat transfer coefficient of the surface of the specimen material, and L is the thickness of the specimen.

Under the given conditions and without considering the transient heat accumulation caused by the constant heat flow, the Eq. (4) is solved, and the function of the temperature response of the specimen with depth and time is

$$T(z, t) = A_w \exp\left(-\frac{z}{\mu}\right) \cos(2\pi f_e t - \frac{z}{\mu}) \qquad (13)$$

where μ is the thermal diffusion length, which represents the physical quantity of the penetration depth of the heat flow in the specimen, and it can be expressed as

$$\mu = \sqrt{\alpha/\pi f_e} \qquad (14)$$

where α is the thermal diffusivity of the specimen.

A_w is the temperature change the amplitude of the specimen's surface, and it can be expressed as

$$A_w = \frac{Q}{2\pi \rho c f_e} \qquad (15)$$

According to Eq. (13), the relationship between the heat flow phase and the depth is

$$\varphi(z) = \frac{z}{\mu} \qquad (16)$$

Thus, the quantitative relationship between the phase difference and the defect depth of the defect area and the defect-free area can be obtained. Besides, according to the empirical rule summarized before, the defect can be detected only when its diameter is at least 2.5–3.0 times its depth [56].

The optical lock-in thermography testing is not affected by uneven heating, and the phase diagram has nothing to do with the emissivity of the specimen's surface. In addition, this technique improves the testing of phase and amplitude, which facilitates the testing and measurement of defects. One disadvantage of this method is that different modulation frequencies must be tried during the testing process. If the frequency is too low, the signal-to-noise ratio (SNR) of the thermography is low, resulting in a much longer single experiment cycle. Conversely, if the frequency is too high, the penetration depth of the thermal flow is not deep enough [36, 57–62].

Structural Optical Scanning Thermography Testing The structural optical scanning thermography testing uses thermal excitations with constant power and different shapes to scan the surface of the specimen. As an emerging thermal excitation method, laser scanning [63] has the advantages of high power density, adjustable pulse width, and uniform energy, so it is often used to generate structural thermal excitation. This paper divides the structural optical scanning thermography testing into three types: the linear scanning thermography testing, the point scanning thermography testing, and the grating scanning thermography testing.
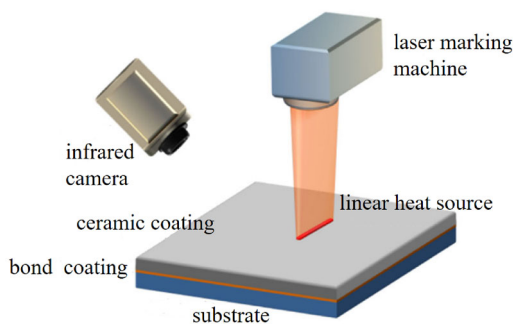
Fig. 5 Schematic diagram of linear scanning thermography testing [65]

Theoretical basis of linear scanning thermography testing

The linear scanning thermography testing is usually used to detect both interface disbond defects and surface crack defects. As shown in Fig. 5, when the linear thermal excitation scans an area on the surface of the specimen at a certain speed, the extremely thin layer of material on the surface of the area is rapidly heated in a short time [64, 65]. After scanning, the rapidly heated area began to dissipate heat, while the heat absorbed by the surface is transferred inside the specimen.

When the linear scanning thermography testing is used to detect interface disbond defects, the lateral diffusion of the heat flow is ignored. Therefore, the linear scanning thermography technique can be considered as the superposition of the optical pulsed thermography technique, so the principle of linear scanning thermography testing is similar to optical pulsed thermography testing.

When the linear scanning thermography testing is used to detect surface cracks, the emissivity of surface cracks of the specimen is higher than in other defect-free areas. Besides, many techniques [66–69] can be adopted to enhance the thermal behavior of cracks. Balageas et al. proposed using the flying spot camera to detect cracks [66, 67]. Salazar et al. [68, 69] realized accurate quantitative detection of cracks by using the laser-spot lock-in thermography. For a rectangular crack with depth D and width W, the emissivity at the crack can be expressed by the following Casselton equation [70]

$$\varepsilon_{\lambda, crack} = \frac{2D + W}{2D\varepsilon_{\lambda, surf} + W}\varepsilon_{\lambda, surf} > \varepsilon_{\lambda, surf} \tag{17}$$

where $\varepsilon_{\lambda, crack}$ is the emissivity of the crack to the light with the wavelength D, and $\varepsilon_{\lambda, surf}$ is the emissivity of the defect-free area on the surface of the specimen. The thermal radiation intensity received by the infrared camera depends on the thermal performance and the emissivity of the surface of the specimen. The specimens and cracks are simplified as gray bodies, and the radiation is considered independent of the wavelength of incident light.

In the case that atmospheric radiation is negligible [65, 71], the radiation N_{cam} received by the infrared camera can be expressed as

$$N_{cam}(x, y) = \varepsilon(x, y)N_{surf}(x, y) + [1 - \varepsilon(x, y)]N_{reft} \tag{18}$$

where ε is the emissivity of the specimen, N_{reft} is the environmental radiation on the surface of the specimen, and N_{surf} is the radiation of the specimen. For specimens with high emissivity, the radiation received by the infrared camera can be approximated to the radiation on the surface of the component. In addition, the influence of N_{surf} can be removed by subtracting the background temperature. When a linear heat source irradiates the surface of the specimen, the surface radiation of the specimen can be divided into two parts: the radiation $N_{surf-heat}$ of the linear heat source heating area and the radiation $N_{surf-back}$ of the unheated area. Similarly, for the surface of the specimen with surface cracks, the emissivity distribution can also be divided into two parts: the emissivity ε_{crack} of the surface crack area and the emissivity ε_o of the defect-free area, and $\varepsilon_{crack} > \varepsilon_o$. When a linear heat source irradiates the surface of a specimen with cracks, the surface environmental radiation N_{surf} is omitted, and the radiation received by the infrared camera can be approximated as

$$\begin{aligned} N_{cam} &= \{\varepsilon\} \times \{N_{surf}\} = \{\varepsilon_o, \varepsilon_{crack}\} \\ &\times \{N_{sur-back}, N_{sur-heat}\} \\ &= \{\varepsilon_o \times N_{sur-back}, \varepsilon_o \times N_{sur-heat}, \varepsilon_{crack} \\ &\times N_{sur-back}, \varepsilon_{crack} \times N_{sur-heat}\} \end{aligned} \tag{19}$$

where $\varepsilon_o \times N_{sur-back}$ represents the radiation of the position where the defect-free area of the specimen is not heated, $\varepsilon_o \times N_{sur-heat}$ represents the radiation of the position where the defect-free area of the specimen is heated, $\varepsilon_{crack} \times N_{sur-back}$ represents the radiation of the position where the cracked area of the specimen is not heated, $\varepsilon_{crack} \times N_{sur-heat}$ represents the radiation of the position where the cracked area of the specimen is heated. In the four parts, $\varepsilon_{crack} \times N_{sur-heat} > \varepsilon_o \times N_{sur-heat} > \varepsilon_{crack} \times N_{sur-heat} > \varepsilon_o \times N_{sur-back}$.

After the calibration of the radiation received by the infrared camera, the temperature distribution T of the specimen is obtained and T can be expressed as

$$\begin{aligned} T(x, y) &= A_0\left(\frac{N_{cam}(x, y)}{\sigma_b}\right)^{-4} \\ &= \zeta(\varepsilon_o \times N_{sur-back}, \varepsilon_o \times N_{sur-heat}, \varepsilon_{crack} \\ &\times N_{sur-back}, \varepsilon_{crack} \times N_{sur-heat}) \\ &= \{T_{0-back}, T_{0-heat}, T_{crack-back}, T_{crack-heat}\} \end{aligned} \tag{20}$$
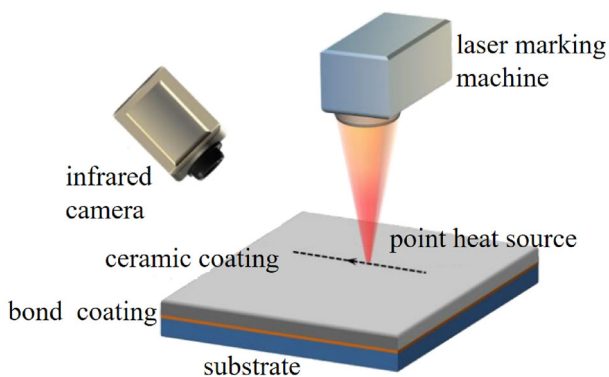
Fig. 6 Schematic diagram of point scanning thermography testing [65]

Fig. 7 Schematic diagram of grating scanning thermography testing [36]

where σ_b is the radiation constant of the black body, A_0 is the fixed parameter calibrated inside the infrared camera, and $\zeta(N_{cam}(x, y))$ represents the temperature distribution of the entire surface when the specimen is heated.

Theoretical Basis of Point Scanning Thermography Testing
As shown in Fig. 6, the point scanning thermography testing [65, 71, 72] is usually used to detect surface cracks. When the thickness of the isotropic material specimen is much smaller than its area, after ignoring the heat conduction in the thickness direction, the two-dimensional Fourier law of heat conduction along the x and y directions on the surface of the specimen can be expressed as

$$q_x(x, y)\vec{i} + q_y(x, y)\vec{j} = -\lambda(x, y)(\frac{\partial T(x, y)}{\partial x}\vec{i} + \frac{\partial T(x, y)}{\partial y}\vec{j})$$

(21)

where T is the surface temperature of the specimen, q is the heat flow density, and λ is the thermal conductivity of the material. Equation (21) shows that under the same heat flow, there will be a higher temperature gradient at a lower thermal conductivity. Under the heating of a point heat source, the arc with the same distance from the heat source has the same heat flow density in the radial direction, and the heat flow density gradually decreases toward the propagation direction. The heat flow density distribution is shown in the following equation

$$q(r, \theta) = \frac{P}{S} = \frac{P}{2\pi r L} = \frac{Q}{r}$$

(22)

where P is the power of the point heat source, θ is the polar angle, r is the distance from a point on the specimen to the center of the point heat source, and S is the heat flow area. For the specimen whose thickness is much smaller than area, $S = 2\pi r L$, where L is the thickness of the specimen. Let
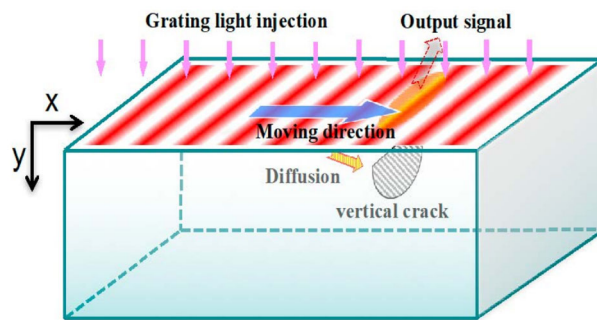
$Q = P/2\pi L$, then

$$q(r, \theta) = \frac{Q}{r}$$

(23)

For the specimen with surface cracks, the thermal conductivity λ distribution of the specimen can be divided into two parts: the surface crack area λ_{crack} and the defect-free area λ_0. Combining Eqs. (21) and (22), the absolute value of the temperature image gradient collected during the point heat source scanning process can be expressed as

$$\left|\frac{\partial T(x, y)}{\partial x}\vec{i} + \frac{\partial T(x, y)}{\partial y}\vec{j}\right| = \frac{\left|q_x(x, y)\vec{i} + q_y(x, y)\vec{j}\right|}{\lambda(x, y)}$$
$$= Q\left\{\frac{1}{r_{\lambda_o}\lambda_0}, \frac{1}{r_{\lambda_{crack}}\lambda_{crack}}\right\}$$

(24)

where r_{λ_0} is the distance from the center of the point heat source to a certain point in the defect-free area of the specimen, $r_{\lambda_{crack}}$ is the distance from the center of the point heat source to a certain point on the crack, $Q/r_{\lambda_0}\lambda_0$ is the temperature gradient in the defect-free area of the specimen, and $Q/r_{\lambda_{crack}}\lambda_{crack}$ is the temperature gradient at the crack.

Theoretical Basis of Grating Scanning Thermography Testing The grating scanning thermography testing uses a sinusoidal linear grating to scan the specimen surface rapidly, forming high-density, pulse-modulated thermal excitation. The advantage of this technique is that at the same frequency, the conduction attenuation of thermal flow signals along the depth direction is faster, and the thermal diffusion depth is smaller [36, 73, 74].

In this method, a series of striped moving light is projected on the surface of the sample, i.e., a light grating with sinusoidal spatial intensity along the x direction, as shown in Fig. 7. The grating wavelength is the distance between two adjacent stripes of light. The incident light moves with a constant velocity along the x direction. After some time, the temperature distribution, due to the injected grating light,

reaches a steady state and it has as the following form

$$T(x, y, t) = T_0 \sin(\frac{2\pi}{l}x - 2\pi f t + \varphi_0) \tag{25}$$

where T_0 is the amplitude of thermal flows at the surface; f is the temporal frequency of the input signal; l is the wavelength of the grating along the x direction at the surface; φ_0 is the initial phase angle. Therefore, this is a moving thermal wave along x direction with a velocity $v = f \times l$.

Controlling the grating wavelength by adjusting the distance of the light gratings through the projector, or the temporal frequency f by changing the moving speed v of the light grating under a fixed grating wavelength l, the thermal wave propagates not only along the y direction, but also along the x direction. When it meets a crack, a reflecting thermal wave will propagate to the surface of the sample. The output signal of thermal flows can be detected by an infrared camera. By adjusting the temporal frequency and moving velocity of the illuminating light in x direction, both the vertical cracks and horizontal cracks can be detected and located. The thermal flow response and thermal diffusivity are followings:

$$\begin{aligned} &T(x, y, t) \\ &= T_0 e^{-y/\eta} \left[\cos 2\pi \left(\frac{y}{\kappa} + \frac{x}{l} - \frac{vt}{l} \right) + i \sin 2\pi (\frac{y}{\kappa} + \frac{x}{l} - \frac{vt}{l}) \right] \end{aligned} \tag{26}$$

where η is the length scale of thermal flow diffusing into the solid, i.e., skin depth; κ is the wavelength of thermal flows in the vertical direction.

Theoretical Basis of Non-stationary Thermal Wave Imaging Testing   The non-stationary thermal wave imaging testing mainly includes the frequency modulated thermal wave imaging (FMTWI) and the quadratic frequency modulated thermal wave imaging (QFMTWI), where QFMTWI can be applied to the coating thickness changes [75–77]. In QFMTWI, a moderate peak power optical stimulus is modulated by a band of low frequencies provided from a set of halogen lamps to the front surface of the object [78]. The expression for quadratic frequency modulated input stimulus is given by

$$Q(t) = Q_0 \sin(at + bt^3) \tag{27}$$

where a is the initial frequency, b is the bandwidth, and Q_0 is the intensity of the heat flux. The applied optical stimulus creates diffusive thermal waves into the subsurface layers of the sample. The one-dimensional heat diffusion equation is the same as Eq. (4), and it can be solved under boundary conditions with quadratic heat flux at the front surface. Therefore, the obtained thermal response in the Laplacian

domain is given by [24]

$$T(x, s) = \frac{T_0}{4\lambda\sigma}(\frac{(1 + R)(1 + Re^{-2\sigma l})}{1 - R^2 e^{-2\sigma l}}) \tag{28}$$

where $\sigma = (1 + j)/\mu$, T_0 is the intensity of thermal wave, and R is the reflection coefficient between coatings and substrate given by $R = (1 - \varepsilon\text{coating})/(1 - \varepsilon\text{substrate})$ since ε is the effusivity of the material and μ is the diffusion length of the thermal wave for QFM given by [24],

$$\mu = \sqrt{\frac{2\alpha}{\pi(a + 3bt^2)}} \tag{29}$$

where α is thermal diffusivity computed from thermo-physical properties of the material. The thermal response in Eq. (28) is subjected to pulse compression by cross-correlating with a reference thermal profile given by

$$T_{corr} = X_{corr}(T * T_{ref}) \tag{30}$$

This results in a correlogram cube by rearranging the compressed profiles in their respective spatial location. The thickness changes from the correlogram are distinguished by the correlation coefficient contrast, and the thickness of each layer is estimated by the correlation peak delays.

2.2.2 Ultrasonic Infrared Thermography Testing

The ultrasonic infrared thermography testing is an NDT technique with ultrasonic waves as the excitation source, so it combines ultrasonic excitation technology with infrared thermography technology. The ultrasonic infrared burst thermography testing [79–82] and the ultrasonic infrared lock-in thermography testing [83–85] are the commonly used ultrasonic infrared thermography testing techniques. Compared with the ultrasonic infrared burst thermography testing that uses the ultrasonic pulse to excite the specimen, the ultrasonic infrared lock-in thermography testing uses the ultrasonic wave modulated by periodic signal amplitude [86, 87].

Theoretical Basis of Ultrasonic Infrared Thermography Testing   In the case of ultrasonic infrared thermography testing, the excitation is accomplished by coupling an ultrasonic transducer, typically, of a horn-type, to the specimen surface. If there is a defect in the specimen, the ultrasonic energy of the high-frequency vibration will cause friction heat at the defect interface. The infrared camera captures changes in the temperature of the specimen's surface, thus detecting the defect. Because the heat is generated through the defect itself, this technique is less affected by background noise and obtains high contrast thermal images. However, in the

process of thermal excitation, the source must transmit ultrasonic energy into the specimen under certain pressure; this pressure could easily cause secondary damage to the object [36, 87].

Friction is the main cause of local heat generation in the defect area when the defect interface is excited by the ultrasonic wave. Assuming that the thermoelastic and hysteresis effects can be neglected, the propagation of ultrasonic waves in thin metal plates can be expressed by the following displacement partial differential control equation (Navier governing equation) [36, 57]

$$(k + \mu)\frac{\partial^2 \mu_i}{\partial x_i^2} + \mu\frac{\partial^2 \mu_i}{\partial x_i \partial x_j} + \rho f_i = \rho\frac{\partial^2 u_i}{\partial t^2} \qquad (31)$$

where μ_i and f_i are the position and volume force tensors, respectively, u is the trimming modulus, k is the lame constant, and ρ is the component density.

The heat flux $Q(t)$ generated by ultrasonic vibration at the contact interface of the defect is calculated by the following equation

$$Q(t) = [u_d + (u_s - u_d)e^{-cv|(t)|}]F_N(t)v_\tau(t) \qquad (32)$$

where $v(t)$ and $v_\tau(t)$ are the relative and tangential velocity of the interface contact point respectively, u_s and u_d are the static and dynamic friction coefficients at the defect, respectively, $F_N(t)$ is the contact force, and c is the velocity coefficient for converting static friction into dynamic friction.

The propagation of the heat flux caused by ultrasonic stimulation at the defect satisfies the heat conduction Eq. (4). Equations (31) to (32) establish an analytical model of acoustic-mechanical-thermal energy coupling for ultrasonic excitation of a metal plate with contact interface defects. Under given initial and boundary conditions, these equations can be solved to obtain changes in the specimen's surface temperature.

2.2.3 Microwave Thermography Testing

According to the excitation configurations of microwave heating, the microwave thermography testing can be divided into microwave pulsed thermography testing, microwave pulsed phase thermography testing, microwave lock-in thermography testing [88], and microwave step thermography testing. Besides, the microwave thermography testing is also known as microwave time-resolved thermography testing [89, 90]. Besides, the heating style of microwave thermography can be divided into dielectric loss heating and eddy current heating [91], therefore the microwave thermography testing can be classified into dielectric loss thermography and eddy current thermography [90–92]. The eddy current

thermography testing has the characteristics of strong penetration, selective heating, volume heating, significant energy saving, uniform heating, and high thermal efficiency. The theoretical basis of microwave thermography testing mainly includes dielectric loss thermography testing and eddy current thermography testing [90].

Theoretical Basis of Dielectric Loss Thermography Testing For dielectric materials, such as glass fiber composite materials, microwave heating is volumetric heating (i.e., dielectric loss heating). Considering glass fiber composites for instance, material dielectric loss in the microwave radiation field will generate heat. The dissipated power P per unit volume can be expressed as follows [90, 93]
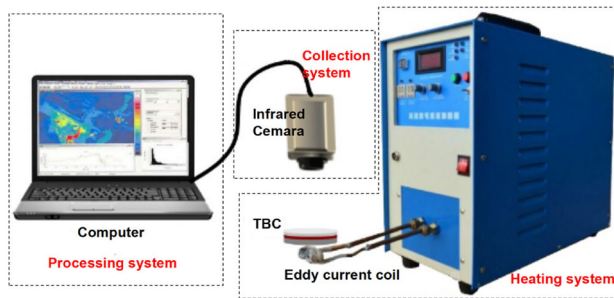
$$P = 2\pi f\varepsilon_o \varepsilon'' E^2 \qquad (33)$$

where f is the frequency of an electric field, E is the RMS value of the electric field, ε_o is the permittivity of air, and ε'' is the relative loss factor. Without considering the heat diffusion, the temperature change per unit at heating time t with a continuous microwave source is [93]

$$T(t) = \frac{Pt}{\rho C_p p} = \frac{\omega\varepsilon_0 \varepsilon'' E^2}{\rho C_p}t \qquad (34)$$

where ρ is the density of the specimen and C_p is heat capacity. Obviously, with constant microwave parameters and constant properties of the specimen, the temperature increases linearly with time. Due to the differences in density and heat capacity between the materials under test and defects, information about surface and internal defects can be obtained.

Theoretical Basis of Eddy Current Thermography For conductive materials, like metals and carbon fiber composites, microwave thermography testing is eddy current thermography testing. According to the relative position of the induction coil and the infrared camera, the eddy current thermography testing can be classified into the eddy current thermography testing under the reflection mode [94–96] and the eddy current thermography testing under the transmission mode [95–97]. The induction heating device and the infrared camera in eddy current thermography testing under the reflection modes are placed on the same side of the specimen, while the induction heating device and the infrared camera in eddy current thermography testing under the transmission mode are placed on both sides of the specimen respectively [98]. Figure 8 is the schematic diagram of eddy current thermography testing under transmission mode. According to the difference in electromagnetic excitation time, the eddy current thermography testing can be classified into pulse eddy current thermography testing and lock-in eddy current thermography testing.

Fig. 8 Schematic diagram of eddy current thermography testing under transmission mode [97]

Fig. 9 Wedge-shaped cracks etched on circular specimen by high-energy laser. **a** Top view. **b** Section view

The eddy current thermography testing involves multi-physical interactions [99] with electromagnetic-thermal phenomena including induced eddy currents, Joule heating, and heat conduction. After being triggered by a signal from a generator, the induction heater generates an excitation signal, which is a period of high-frequency alternating current with high amplitude. The current is then driven into an inductive coil positioned on a sample at a small distance. When the current passes through the coil, it induces eddy currents in the specimen. These eddy currents are governed by a subsurface penetration depth δ, based on an exponentially damped skin effect. The latter can be calculated from

$$\delta = (\pi u \sigma f)^{-1/2} \tag{35}$$

where f is the frequency of the excitation signal, σ is the sample electrical conductivity, and u is the magnetic permeability of the sample. The temperature of conductive material increases due to resistive heating from the induced eddy current, which is known as Joule heating. It can be expressed as

$$Q = \frac{1}{\sigma}|J_s|^2 = \frac{1}{\sigma}|\sigma E|^2 \tag{36}$$

where the sum of generated heat Q is proportional to the square of the eddy current density J_s. The heating style for metallic materials is surface heating [92]. The resistive heat will diffuse as a time transient until a heat balance is restored between the bulk and its surface, at which time the signal will come to a steady state. The heat diffusion process is governed by Eq. (4). In this process, the temperature field on the surface of the specimen will be captured by the infrared camera.

When an induced eddy current encounters geometric discontinuity or local anomalies, the eddy current will be forced to divert, resulting in distorted regions of eddy current densities. The eddy current diversion leads to heat distribution with different thermal contrasts between defective and defect-free areas, which makes the defect visible using the infrared camera [100].
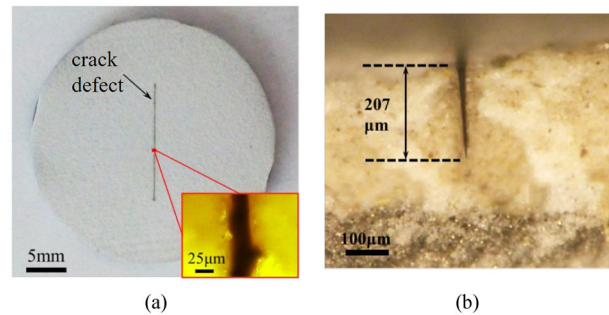
3 Fabrication Techniques of Artificial Cracks and Disbond Defects

After TBCs have been in service, surface crack defects and interface disbond defects are diverse and complex in distribution. For those who want to effectively evaluate the advantages and applicability of crack defects and disbond defects testing technology, the real defects would bring many interfering factors. Therefore, it is necessary to fabricate representative surface cracks and disbond defects with known parameters as the basis for evaluating NDT techniques in TBC. This section reviews the artificial fabrication methods for surface cracks and internal disbond defects in TBCs.

3.1 Fabrication Techniques of Artificial Cracks

In the fabrication of cracks for TBC, especially the ceramic top coat, the tensile fatigue is often used to fabricate surface cracks. In addition, by changing the parameters of the ceramic top coat spraying process, such as shortening the distance between the spray gun and the specimen to change the size and shape of the ceramic particles, the density and depth of the cracks can also be controlled within a certain range [101–103]. The literature [104] proposed to use of a high-power CO_2 laser to scan the surface of the ceramic top coat. Due to the hard and brittle phase of the ceramic top coat and the internal residual stress, cracks will form in the ceramic top coat during the cooling stage. The literature [105] used mechanical cutting to fabricate cracks with a width of 100 μm or more.

To accurately locate and quantify artificial cracks, Liu et al. [65] used a narrow high-energy laser to etch the surface of the specimen, which could fabricate a suitable wedge-shaped crack. As shown in Fig. 9, the semiconductor laser marking machine was used to etch a wedge-shaped crack with a width of 30 μm and a depth of 207 μm on a circular specimen with a diameter of 30 mm and a ceramic top coat
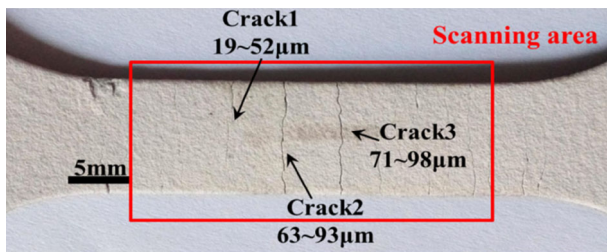
Fig. 10 TBC specimen with three main cracks made by mechanical stretching [65]

of 250 μm. The numerical control equipment of the semi-conductor laser marking machine can control the position, shape, and depth of the artificial crack.

In addition, it is necessary to fabricate TBC's cracks that are closer to the real situation for the research of crack detection in the actual environment. Liu et al. [65] fabricated surface cracks on the TBC specimen by mechanical stretching method using TBC tensile specimens. As shown in Fig. 10, the TBC specimens used here were conventional plasma-spray deposited coating structure, which consisted of a substrate of nickel base alloy, bond coat, and ZrO_2 ceramic coat, and their thickness are 2000, 100, and 400 μm, respectively.

3.2 Fabrication Techniques of Artificial Disbond Defects

The artificial fabrication technique of real disbond defects plays an important role in the development of NDT in TBCs, and the difficulty is that it occurs inside the TBC specimen.

Grzegorz Ptaszek et al. [19] proposed an artificial disbond that provided a better representation of a real disbond of a certain diameter. A flat bottomed hole was modified by tapping it and introducing a screw made of the same material as the substrate. The screw thread was filled with thermally conductive metal grease so the material below the disbond was effectively re-instated. Lateral heat flow below the disbond could therefore occur, as with the real disbond. Heat could also flow through the small air gap in the disbond, where the thickness was controlled by the size of the quartz grain.

The above technique can fabricate internal disbond defects, but in the specific production process, the following issues may affect the fabrication effect and cost: (1) when drilling screw holes on the structure that has been sprayed with TBC, the ceramic top coat may be damaged during the drilling process, resulting in the scrapping of the specimen; (2) Due to the high hardness of the super-alloy substrate, the diameter of the screwed hole is difficult to be further reduced, making it impossible to observe the temperature response of smaller size disbond defects;

Therefore, as shown in Fig. 11, Liu et al. [65] developed a new fabrication technique for disbond defects. The detailed process is as follows: (1) a screwed hole was drilled in the 202 stainless steel substrate; (2) a screw matching the screwed hole was filled; (3) the excessed part of the screw was removed by mechanical cutting; (4) the upper surface of the screw was polished to be flush with the upper surface of the substrate; (5) the upper surface of the specimen was mechanically shot peened to form a plastic surface; (6) the ceramic top coating were sprayed on the upper surface of the specimen, and the thicknesses is 400 μm; (7) the screw was loosened to form the air coating, and a TBC specimen with artificial disbond defects is fabricated. When the screw was fully removed from the threaded hole, a TBC specimen with a blind hole defect was also prepared. Using this fabrication method, the sample with artificial disbonds and the sample with blind holes are made, as shown in Fig. 12a–c. The dimensions of their substrates are $50 \times 40 \times 2$ mm^3, and the diameters of the defects are 2 mm and 3 mm. The detection results of the blind hole and disbond defect measurements are shown in Fig. 12d and e.

A real TBC containing disbond defects generally meets the following conditions: (1) neither the super-alloy substrate nor the ceramic top coat is damaged, and the two are separated in the disbond area; (2) no interface disbond defects can be found on the surface of the TBC; (3) The thermal conductivity of the filler at the interface between the super-alloy substrate and the ceramic top coat is close to that of air.

To make the artificial disbond defect closer to the real interface disbond defect, Liu et al. [102] proposed a new technique for fabricating disbond defects, namely the ceramic hollow particle embedding technique. As shown in Fig. 13, the specific process of the fabrication technique was as follows: (1) the schematic diagram of super-alloy substrate (Fig. 13a); (2) the metal substrate surface was subjected to mechanical shot peening to form a plastic surface (Fig. 13b). (3) after shot peening, a bond coat was sprayed on the surface (Fig. 13c). (4) the laser marking machine was used to engrave the same groove as the prefabricated disbond defect on the bond coat (Fig. 13d). (5) the optimized mixture with high-temperature ceramic hollow particles and high-temperature glue was poured into the area where the bond coat was removed (Fig. 13e). (6) the zirconia ceramic coat was sprayed onto the specimen surface (Fig. 13f).

Before the fabrication, an ultrasonic device was used to crush part of the particles, and then particle debris samples were made to prove the internal hollow of the ceramic particles and the feasibility of using ceramic particles as an alternative to the air layer. The complete ceramic hollow particles and the destroyed ceramic hollow particles were observed with an optical microscope. The complete ceramic hollow particles after being magnified 500 times are shown in Fig. 14a, and a destroyed ceramic hollow particle is

Fig. 11 Process of fabricating disbond defects
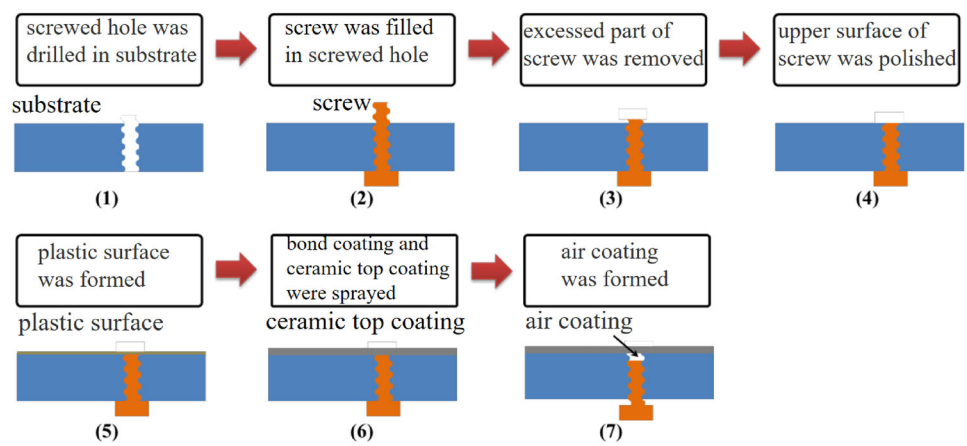
Fig. 12 TBC samples with two kinds of defects and detection results. **a** Subface of blind hole defects. **b** Subface of artificial disbond defects. **c** Surface of ceramic coating in both samples. **d** NDT result of TBC sample with blind holes. **e** NDT result of TBC sample with artificial disbands [108]
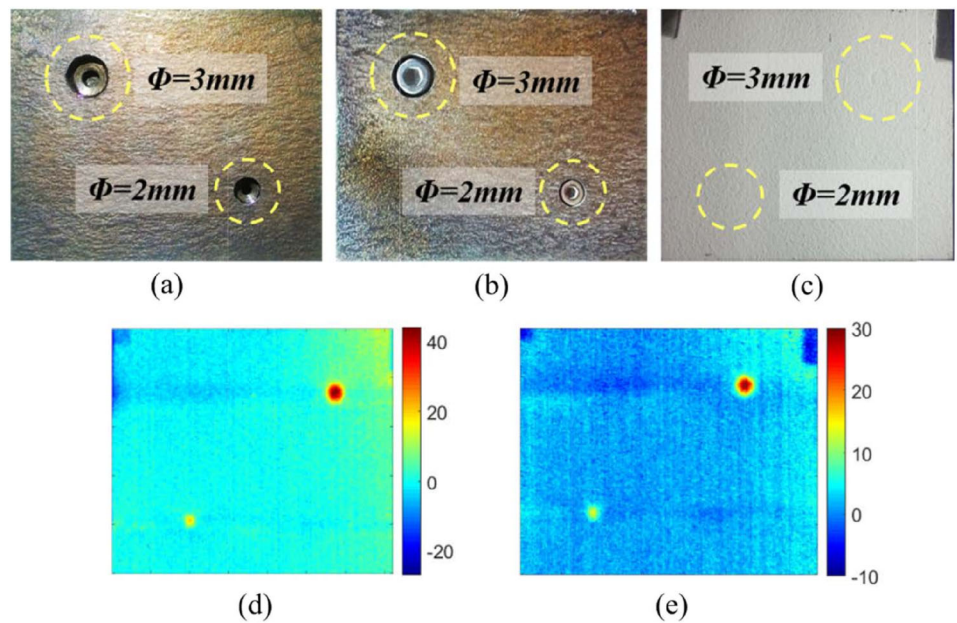
**Fig. 13** Specific process of fabrication technique [107]
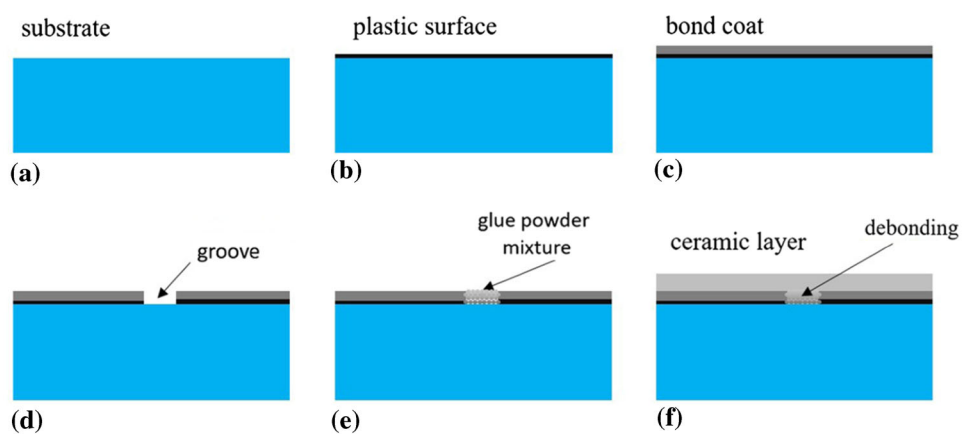
shown in Fig. 14b. By changing the depth of field, the three-dimensional microscopic images in Fig. 14c of the ceramic

hollow particles are obtained. As shown in Fig. 14c, the artificially destroyed ceramic hollow particle fragments are a hollow hemisphere.

Fig. 14 Observation of particle debris samples in optical microscope. **a** Complete ceramic hollow particles. **b** Destroyed ceramic hollow particle. **c** 3-D microscopic image of ceramic hollow particle [107]
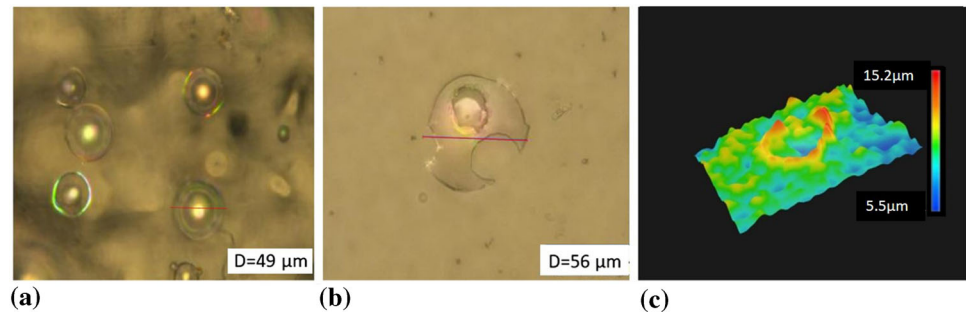
Fig. 15 Artificial interface disbond defect. **a** Surface of specimen after removing part of the bond coat. **b** Surface of specimen filled with ceramic hollow particle mixture. **c** Surface of specimen sprayed with the ceramic top coat
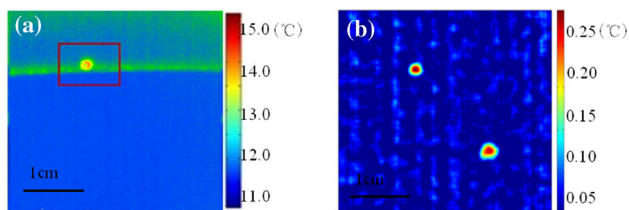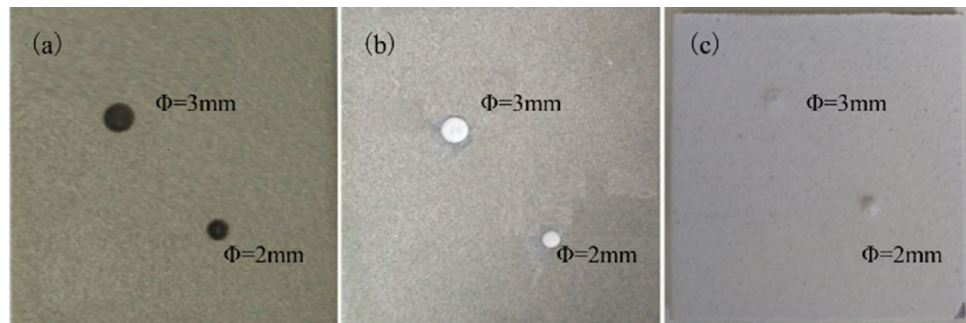
Fig. 16 Detection results of disbond defects by linear scanning thermography testing. **a** Raw thermal image. **b** Thermal image processed by line laser carrier algorithm
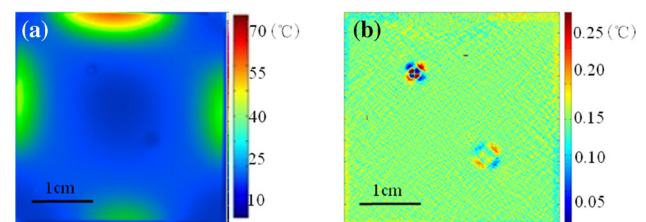
Fig. 17 Detection result of disbond defects by eddy current thermography testing. **a** Raw thermal image. **b** Gradient thermal image processed by adaptive carrier algorithm

The artificial interface disbond defect made on the flat substrate with super-alloy was shown in Fig. 15. Figure 15a was the surface of the specimen after the laser marking machine removed part of the bond coat. Figure 15b was the specimen filled with a ceramic hollow particle mixture. Figure 15c was the specimen sprayed with the ceramic top coat.

The detection result of the disbond defect shown in Fig. 15 by linear scanning thermography testing is shown in Fig. 16. The thermal image when the line laser scans to the disbond defect is shown in Fig. 16a, and the thermal image processed by the line laser carrier algorithm are shown in Fig. 16b. The detection result of the disbond defect shown in Fig. 15 by eddy current thermography testing is shown in Fig. 17. The thermal image obtained by eddy current thermography testing is shown in Fig. 17a, and the gradient thermal image processed by the adaptive carrier algorithm is shown in Fig. 17b.

In addition to plane specimens, Liu et al. [97] also used the ceramic hollow particle embedding technique to fabricate artificial interface disbond defects on real blades with

large surface curvature, complex shapes, and uneven thickness distribution. The artificial interface disbond defect made on the real blade as shown in Fig. 18. Figure 18a–e were the super-alloy blade, the blade with the surface shot peening, the blade sprayed with the bond coat, the blade filled with the ceramic hollow particle mixture, the blade sprayed with the ceramic top coat, respectively.

Figure 19 showed a real blade containing two artificial interface disbond defects and the raw thermal images obtained by eddy current thermography testing.

4 Application Status of Various Active Infrared Thermography NDT Techniques in TBC

This section reviews the state-of-the-art application status of various active infrared thermography NDT techniques in

Fig. 18 Artificial interface disbond defect on real blade. **a** Super-alloy blade, **b** Blade with surface shot peening. **c** Blade sprayed with bond coat. **d** Blade filled with ceramic hollow particle mixture. **e** Blade sprayed with ceramic top coat
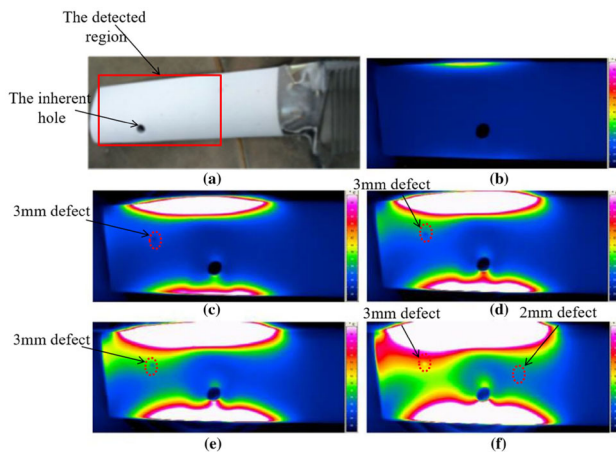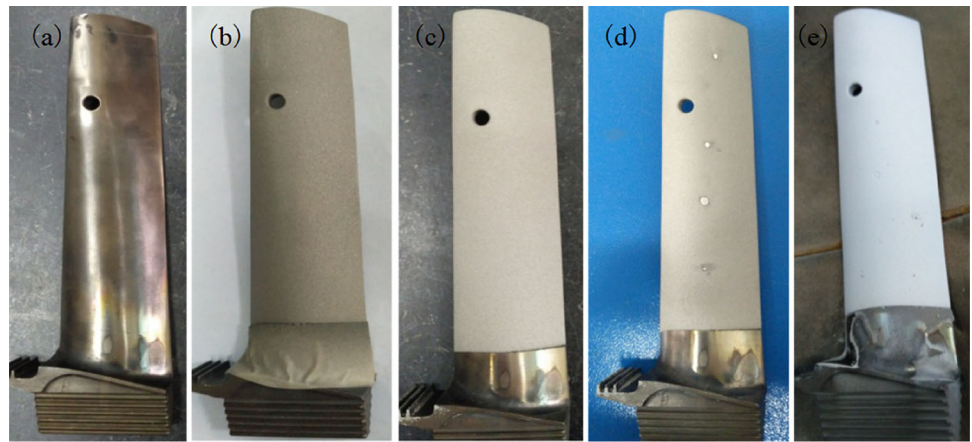
Fig. 19 Thermal images of real blade with artificial interface disbond defects at different times. **a** Image at 0 s. **b** Raw image at 0.4 s. **c** Image at 0.8 s. **d** Image at 1.2 s. **e** Image at 1.6 s. **f** Image at 2 s [97]

the three aspects of TBC's interface disbond defects detection, surface crack defects detection, and coating thickness detection, and compares the application and characteristics of various active infrared thermography NDT techniques.

## 4.1 Surface Crack Defects NDT

The structural optical scanning thermography testing is mainly applied to TBC's surface crack defects detection.

For detecting surface cracks in TBCs, Liu et al. [65] developed a laser multi-modes scanning thermography testing technique, as shown in Fig. 20, combining linear scanning thermography testing technique and point scanning thermography testing technique. Figure 20a was the schematic of the linear heat source in the vertical scan stage, Fig. 20b was the linear heat source in inclined scan stage, Fig. 20c was the linear heat source in the parallel scan stage, Fig. 20d was the point heat source in fine scan stage.

Besides, they found that the changes in the thermal physical parameters at the cracks caused the temperature image to show 5 features. In the process of vertical scanning, the direction of linear laser scanning and heating was perpendicular to that of crack length (Fig. 21a). Since the radiation coefficient at the crack was higher than in other positions, meanwhile, the crack surface area available to adsorb heat was also larger than other normal regions, thus the temperature at the intersection position of the linear heating source and crack had a significant rise (Feature 1, Fig. 21b). The heat dissipation rate at the crack was slower than in other positions, which made the temperature image change near the crack, generating high residual temperature after linear laser scans of the crack. A 'tailing' phenomenon behind the linear laser appeared for a relatively long moment along with the linear laser scanning going through the whole crack defect (Feature 2). In the process of inclined scanning, the linear laser is scanning at a certain inclined angle with the crack. It was worth noting that, apart from a higher temperature region at intersecting location between the linear laser and the crack, another obvious phenomenon, 'dislocation' in temperature images near the crack, often occurred for inclined scanning (Feature3). This was because the upper end surface and the lower end surface of the crack were disconnected and discontinuous, in which thermal conductivity was blocked and drastic changes. When scanning on the crack, the linear laser was heating on different stagger positions of the upper end surface and lower end surface, respectively. These reasons above caused the 'dislocation' phenomenon in the temperature image. In addition, a 'tailing' dragged behind the linear laser during inclined scanning was also distinct. In the process of parallel scanning, when the linear laser had scanned the crack, the temperature at the overlapping region elevates to the highest. The area with high temperature increases to the peak after the linear laser just scanned through the crack and the dragged phenomenon also occurs (Feature 4). In the line-scan stage, vague shape and low contrast in temperature images with slightly high temperature might appear usually
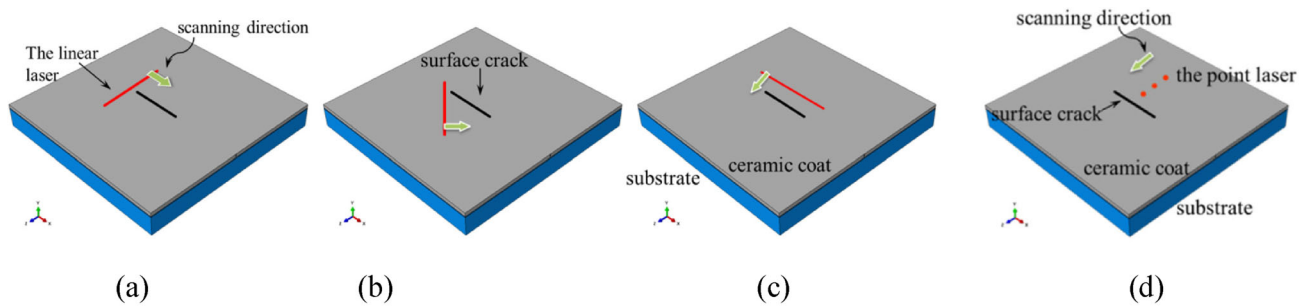
Fig. 20 Scanning schematic of laser multi-modes scanning thermography testing technique. **a** Linear heat source in vertical scan stage. **b** Linear heat source in inclined scan stage. **c** Linear heat source in parallel scan stage. **d** Point heat source in fine scan stage [65]
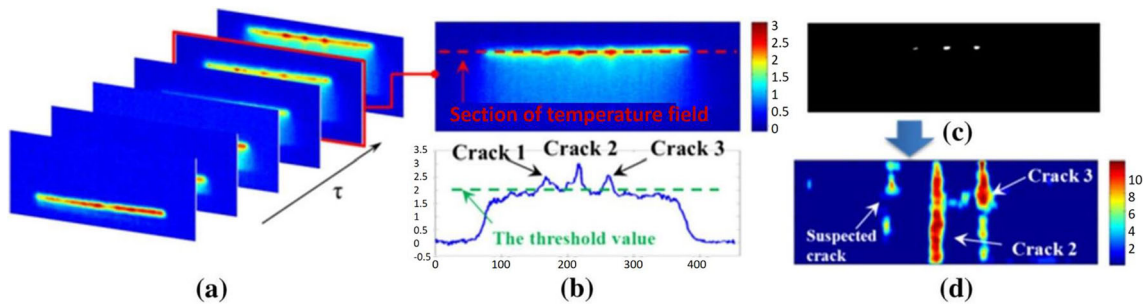
Fig. 21 Reconstruction process of three cracks in vertical scanning. **a** Original temperature images in time series. **b** Temperature image at a certain moment and its temperature distribution in one section. **c** Threshold extraction result at this moment. **d** Reconstruction result [65]
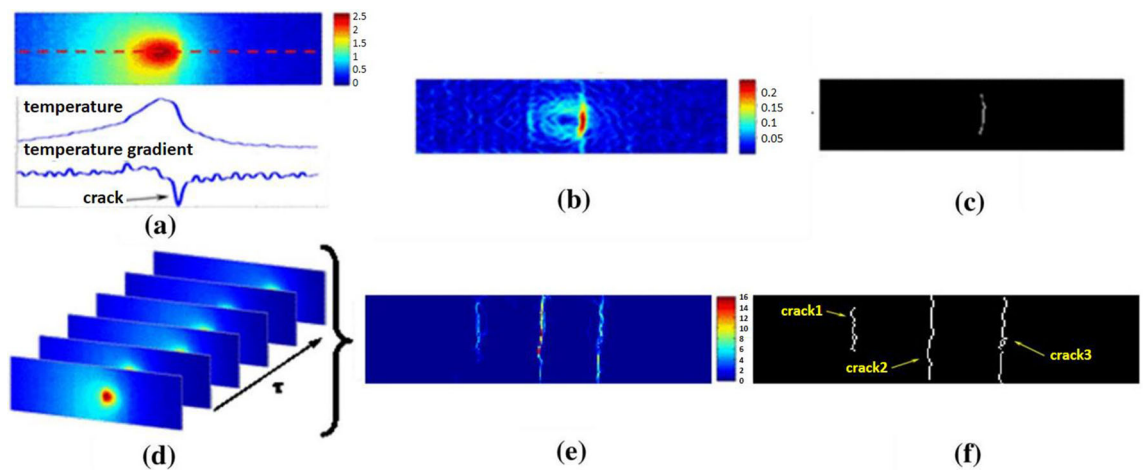
Fig. 22 Process of point laser scanning stage. **a** Temperature image at a moment (above), temperature section (middle) and temperature gradient (below). **b** Gradient distribution of temperature filed at a moment. **c** Thinning the binaryzation result of the temperature gradient at a moment. **d** Original temperature images in time series. **e** Accumulation result of temperature gradient at each moment. **f** Final result by combining rough scanning with fine scanning [65]

due to the narrow width of the tested crack and low resolution of the infrared camera. For these suspected defect regions, the point-scan method was developed to further ascertain them. Therefore, when the point heat source was close to the crack, the thermal obstruction phenomenon became more obvious (Feature 5, Fig. 22a).

Taking the vertical scanning as an example, the cracks reconstruction process and the final result were shown in Fig. 21. Figure 21a was the original temperature images in the time series. Figure 21b was the temperature image at a certain moment and its temperature distribution in one section. Figure 21c was the threshold extraction result at this moment. Figure 21d was the reconstruction result.

When a point laser moved toward the micro-crack in a certain direction, the heat conduction would be impeded by the crack (upper image in Fig. 22a), and the temperature gradient value near the crack would have a significant abnormality (lower image in Fig. 22a). Figure 22b was the full field temperature gradient image, and after thinning the binarization result of the temperature gradient (Fig. 22c), the shape and location of the suspected crack could be visually presented. By accumulating all of such thinning results of temperature gradient binarization for all temperature images in time series and combining them with the results of linear laser scanning, all cracks could be displayed in the scanning range, as shown in Fig. 22d–f.

Cernuschi et al. [106] obtained a semi-quantitative estimation of cracks at the TBC interface from thermal diffusivity values measured on coupons subjected to thermal cycling using the active infrared thermography technique. For each sample, the thermal diffusivity was measured at fixed lifetimes, and the evolution of the cracked fraction of the interface was estimated by adopting a two-dimensional inversion model.

4.2 Interface Disbond Defects NDT

The optical infrared thermography testing and eddy current thermography testing are mainly applied to TBC's interface disbond defects detection.

Liu et al. [107] developed a linear scanning thermography testing technique for locating disbond defects in blades coated with TBCs, and the linear scanning thermography testing technique was shown in Fig. 23. Compared with planar specimens, the uneven temperature distribution in the blade surface was an unavoidable problem when using a line heat source because the complex shape of the blade made the heat absorbed non-uniform. This unevenness shielded the thermal response features of the defects and disturbs the identification of the defects. The developed window-averaged carrier post-processing algorithm could solve this problem to achieve NDT of disbonds. As shown in Fig. 24, the process was as follows: (1) the raw temperature image of each frame was collected by the infrared camera (Fig. 24a); (2) the background image was subtracted from the raw temperature image, and then the blank area was cropped to reduce the processing area (Fig. 24b); (3) the line heat source was extracted from the forefront of line heat-source scanning (Fig. 24c); (4) the averaged carrier temperature field was constructed within the window area (Fig. 24d); (5) the carrier temperature field was subtracted from the actual temperature field with the defect information, and the position of the disbond defect is displayed (Fig. 24e); (6) the subtracted temperature field images were accumulated at all moments, following the time series (Fig. 24f); (7) threshold segmentation was done

in the final temperature image to further remove the noise (Fig. 24g).

Liu et al. [108] used blind hole defects as substitutes for Interface disband. The linear scanning thermography testing technique was developed in this study and combined with several post-processing algorithms to accurately detect blind hole defects in TBCs. The detailed process was as Fig. 25. After calculating the temperature amplitude of every pixel and constructing the oriented carrier amplitude in the computational window, the amplitude image with the thermal response of the defect is obtained by subtracting the oriented carrier (Fig. 25a). By superposing such amplitude images at all moments, the resultant thermal image with the defects in the whole field is obtained (Fig. 25b and c). The final black and white binary image after threshold extraction is shown in Fig. 25d.

When the eddy current thermography testing technique is used to detect the artificial disbond defects in TBCs samples, the temperature distribution of specimen surface is uneven on account of geometric heating effect, skin effect, edge effect, and abnormal emissivity. The uneven temperature distribution shields the weak thermal response characteristics of the defects and interferes with the identification of the defects. Liu et al. [97] established adaptive carrier algorithms to resolve this problem. With the use of the proposed post-processing algorithm, the thermal images only including the blind-hole defect response are generated and shown in Fig. 26. Figure 26a was the resultant thermal image of the first kind of TBC sample with 3 and 2 mm blind holes. Figure 26b was the resultant thermal image of the second kind of TBC sample with 3, 2, and 1 mm blind holes. Figure 26c was the resultant thermal image of the second kind of TBC sample with a 0.5 mm blind hole.

Ptaszek et al. [109] found that non-uniform energy absorption caused by the non-uniform color of TBC affects the thermal contrast from defects and it might also generate false indications of defects. However, the problem of non-uniform color could be eliminated if the 2nd derivative of surface cooling on a log–log scale was applied as a signal processing technique. This technique combined with the optical pulsed thermography testing was applied to enhance disbond detection in TBC systems and helps to eliminate false indications of defects.

Tang [110] used optical pulsed thermography testing technology to quantitatively detect disbond defects' diameter and depth in TBCs. By combining principal component analysis with neural network theory, the Markov-PCA-BP algorithm was proposed. In the prediction model, the principal components which could reflect most characteristics of the thermal wave signal were set as the input, and the defect depth and diameter were set as the output. The experimental result showed that both the defect depth and diameter were identified accurately, which proved the effectiveness of

Fig. 23 Line heat- source scanning thermography system [107]
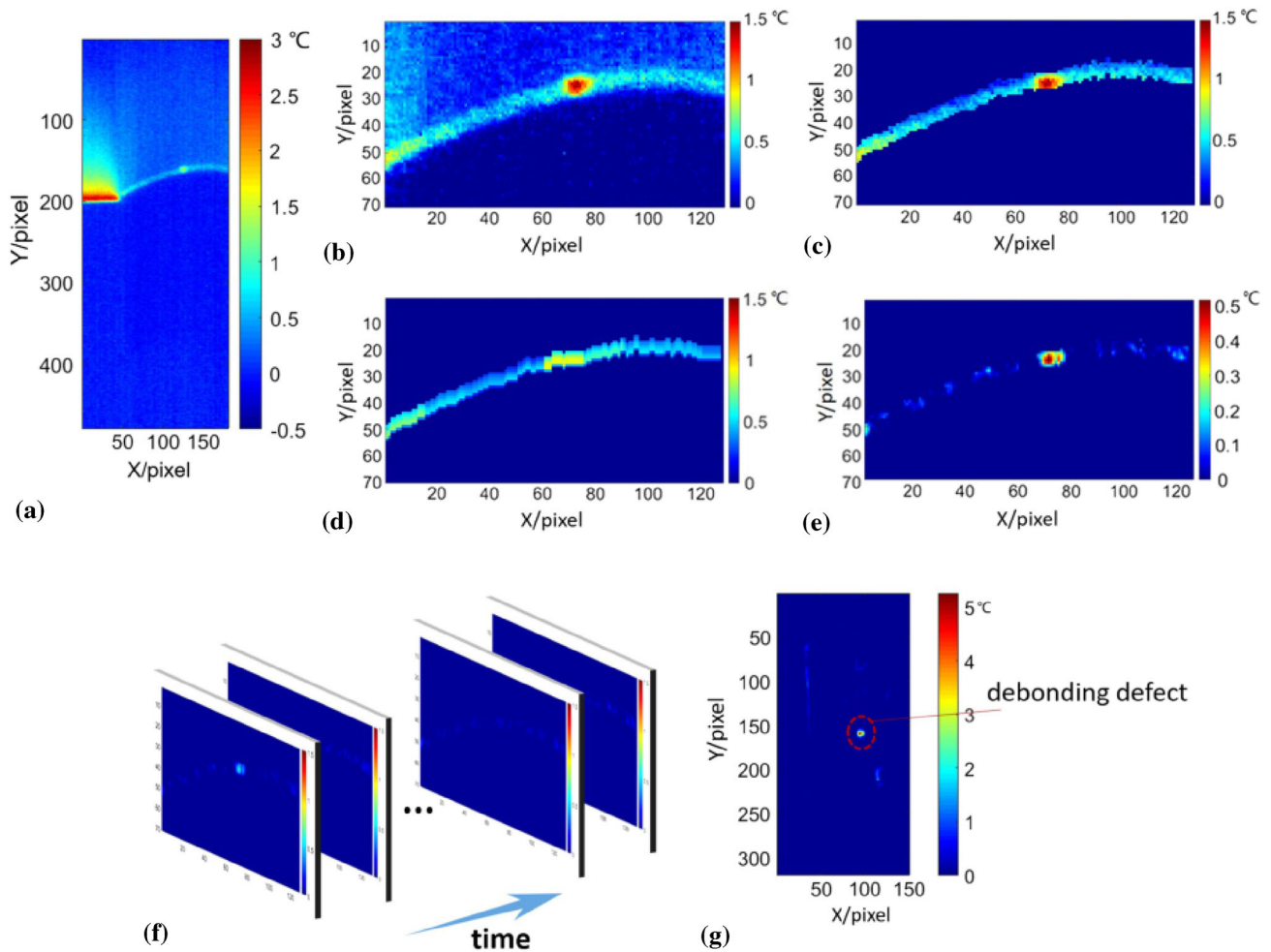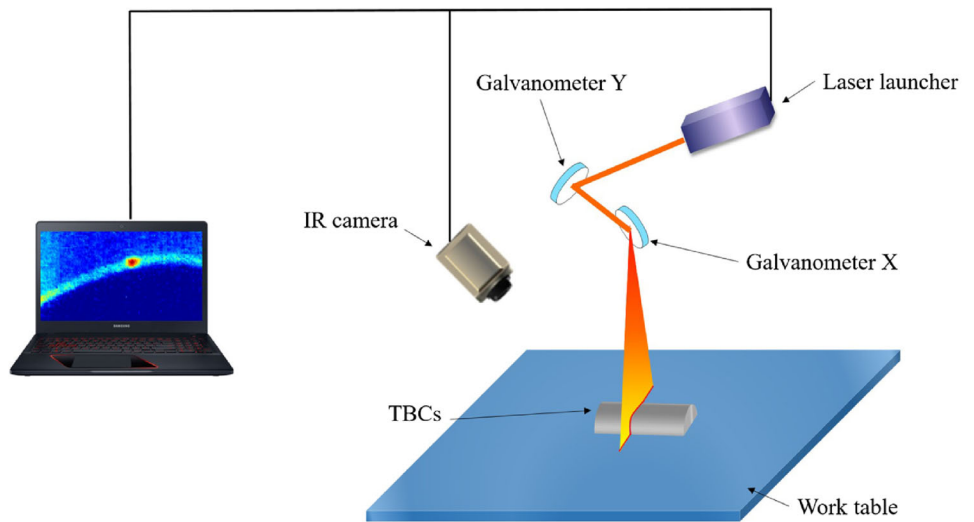
Fig. 24 Process of window-averaged carrier post-processing algorithm [107]

Fig. 25 Process of three-moment windowing amplitude algorithm. **a** Amplitude image with thermal response of defects obtained by subtracting the oriented amplitude carrier; **b** Superposing such subtraction amplitude images at all moments; **c** Resultant thermal image with defects in the whole field; **d** Threshold extraction result [108]
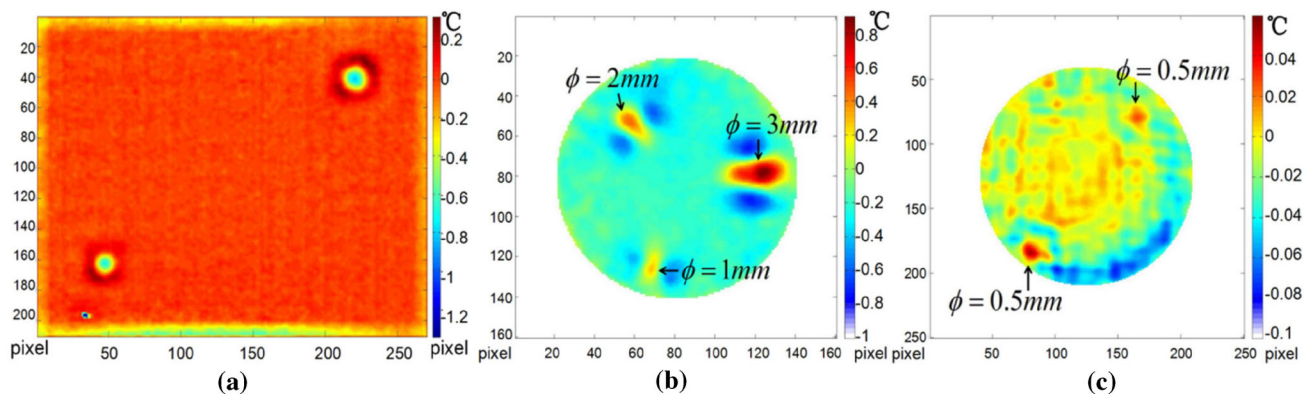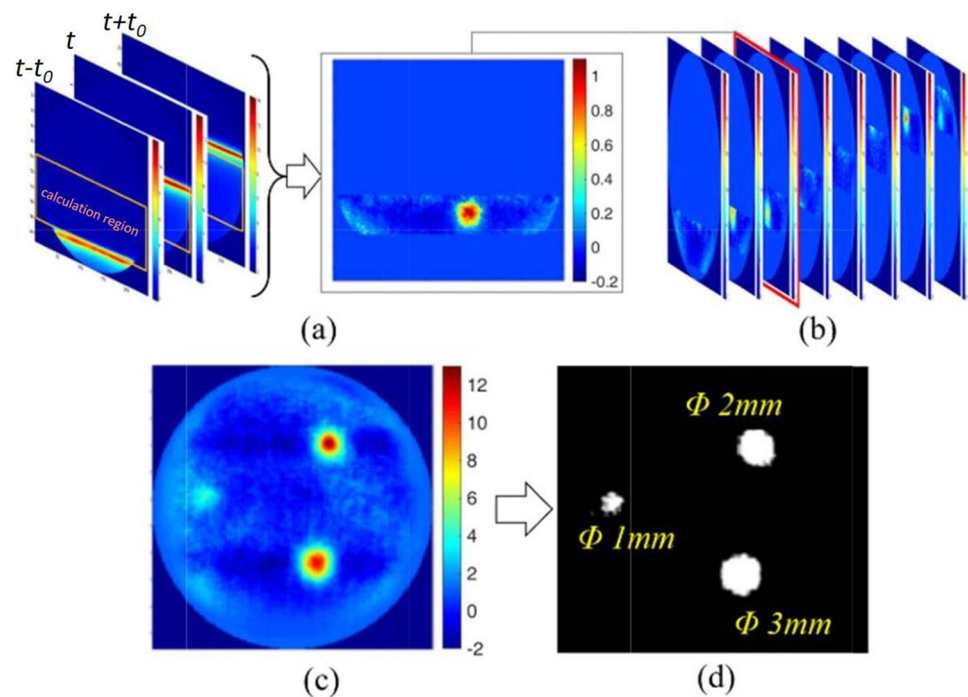
Fig. 26 Thermal images of blind-hole defect response. **a** Thermal image of TBC sample with blind hole without substrate after post-processing. **b** Thermal image of TBC sample with blind hole with metal after post-processing. **c** Thermal image of circular TBC sample with blind hole of 0.5 mm with metal after post-processing [97]

the proposed method for quantitative detection of disbond defects in TBCs.

They also used optical pulsed thermography testing technology to conduct experimental research on Yttria-stabilized zirconia TBC structure disbond defect detection [111]. Differences between surface temperature signals of sound and defective regions, detection effect comparison of heating and cooling process, detection effect comparison of different defect preparation methods, and impact of inspection parameters on detection effect were studied and discussed.

Besides, Tang et al. [112] used the singular value decomposition (SVD) method for infrared image sequence reconstruction, and the component of surface temperature signal feature information had been extracted. Compared to the

original image, the contrast and signal-to-noise ratio of the reconstructed image have been improved. Canny, LOG, and other classical edge detection operators were used to detect the edge of infrared images, and their detection results were compared and analyzed. Based on analyzing the effect of the classical edge detection operators on the defect edge recognition in infrared images, a hybrid algorithm for edge detection based on the Retinex-watershed-Canny operator is proposed for image edge detection, and the thermal barrier coating structure disbond defects' edge has been recognized.

Tang et al. [113] overcame the shortcoming of the shallow inspection depth in optical lock-in thermography testing, and the disbond defects could be detected by using optimized experimental parameters.
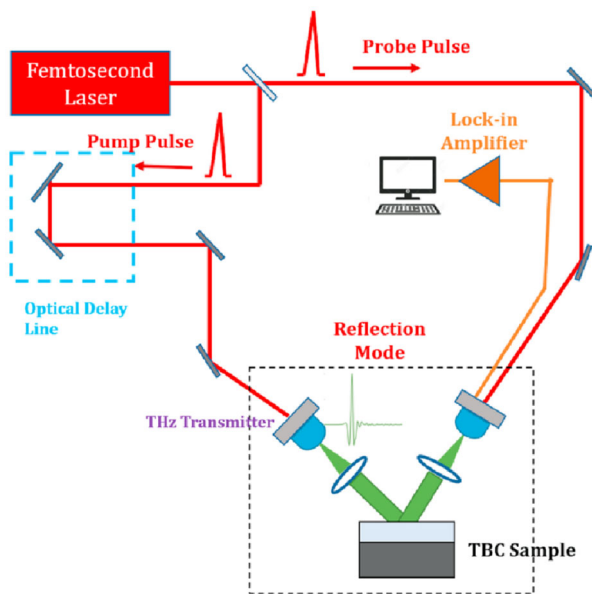
Fig. 27 Schematic of THz-TDS system employed in this study [115]

4.3 Coating Thickness NDT

The optical pulsed thermography testing and the optical lock-in thermography testing are mainly applied to TBC's coating thickness detection.

When performing in-field tests on TBCs deposited on turbine blades, the coating thickness changes, which are not regarded as anomalies, are one of the most common sources of false alarms. They are very challenging to recognize because, unlike stains, eroded areas, and optical property variations, they are not detectable in the visible band. Furthermore, their thermal signal is similar to the one produced by an adhesion defect. In this paper, Therefore, Marinetti et al. [114] proposed an approach based on the analysis of the apparent effusively profile to reliably discriminate thickness changes and real defects.

As shown in Fig. 27, Sreedhar et al. [115] used optical pulsed thermography testing and Terahertz-Time Domain Spectroscopy (THz-TDS) techniques to evaluate the degree of degradation of the thin APS TBCs' top coat thickness. A simplified analytical model was used to aid calibration and development of a regression model to quantitatively analyze the thickness degradation in real-world TBC samples that have endured varying service life, and these measurements were later verified using THz-TDS imaging.

Zhang et al. [24] performed an in-depth study on the application of lock-in thermography in TBC coatings inspection through numerical modeling and analysis. The numerical analysis helped explore the relationship between coatings thickness and phase, and the relationship laid the foundation for the accurate calculation of coatings thickness.

Sahnoun et al. [116] used optical pulsed thermography testing for the coatings thicknesses evaluation in TBCs. They treated the laser-pulsed thermography data with neural networks to model the relationship between the thermal response and the coating thickness. Indeed, the initial weights of the network found and the number of data processed facilitated the convergence of these algorithms. The proposed hybrid model gave a good accuracy in estimating the thin thicknesses of TBCs with deviations less than 3%.

Tang et al. [117] used the optical pulsed thermography testing technology to carry out TBC uneven thickness detection. A three-dimensional heat conduction model of pulsed heat in the coating structure was built, based on which finite element method simulation was done, and the influence of coating thickness, sampling frequency and sampling time was analyzed.

Because of the key role played by thickness and low thermal diffusivity of TBC in the decreasing of the substrate material temperature, both delaminations and thickness variation must be detected and classified. Bison et al. [118] presented a specific study on the detection performances of optical pulsed thermography testing, even when a non-uniform TBC thickness was superimposed to the disbond defect.

TBCs are typically translucent to visible light and near-infrared infrared radiation, so that incident light at the surface permeates the coating. The degree of translucence is specific to the coating composition and thickness. For the service lifetime, coating translucence will decrease as the part is subject to extremely high temperatures. Long term changes in translucence may be due to charring of the coating surface, or more fundamental changes to the coating, including loss of thickness. Shepard et al. [119] processed the resulting time sequence using the thermographic signal reconstruction obtained by the optical pulsed thermography testing technology to generate thickness maps which were accurate to an accuracy of a few percent of the actual coating thickness in TBCs. Optical translucence in newly manufactured coatings was investigated using a set of free-standing TBCs (8 wt% yttria stabilized zirconia subjected to alumina particle jet erosion). Coatings ranging in thickness from 6–60 mils were placed between a white light source and a visible CCD camera, which measured the transmitted signal. Transmission decreased with thickness, consistent with exponential absorption.

As shown in Fig. 28, Shrestha et al. [120] investigated the possibilities of evaluating non-uniform TBC coating thickness using the thermal wave imaging (TWI) method. A comparative study of optical pulsed thermography testing and optical lock-in thermography testing based on evaluating the accuracy of predicted coating thickness was presented. In this study, a transient thermal finite element model was created. The response of the thermally excited surface was

Fig. 28 Principle of evaluation of coating thickness with TWI [120]
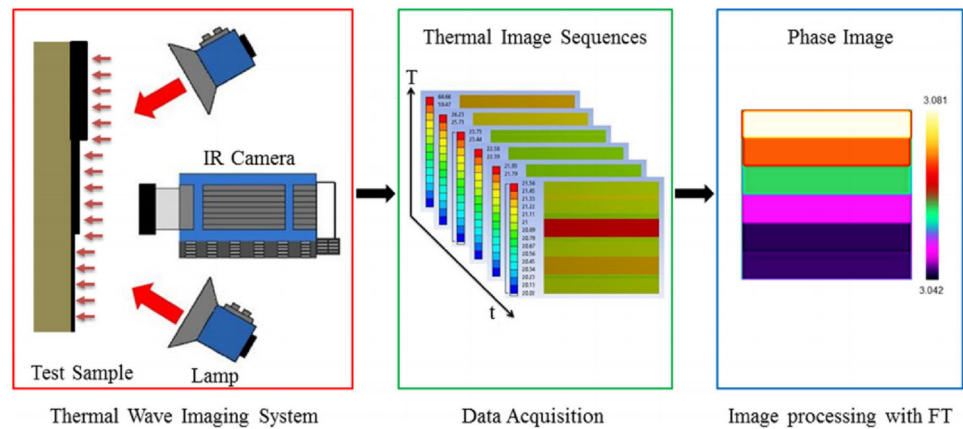
recorded and data processing with Fourier transform was carried out to obtain the phase angle. Then calculated phase angle was correlated with the coating thickness.

Muzika et al. [121] proposed a fast contactless measurement of a paint thickness non-uniformity using flash pulse thermography. Specimens sprayed by a paint were thermally excited by a flash lamp and temperature responses were recorded with an infrared camera. The recorded sequences were post-processed with Fast Fourier Transform to obtain phase angles. Differences in the resulting images showed phase differences which corresponded to a paint thickness non-uniformity. Furthermore, the phases were correlated with the thickness using a calibration curve so that the paint thickness could be determined with flash pulse phase thermography measurement.

Zhao et al. [64] adopted the optical thermography testing technique and the logarithmic peak second-derivative method to measure the thickness of top coat in TBCs. Time dependent thermal images were used to characterize the microstructure which was confirmed by scanning electron microscope.

Ghali, V. S. et al. [75] modeled a thermal barrier coatings sample with uniform thickness variations, excited with the QFMTWI. With the pulse compression employed over the resultant thermal response, the coating thickness resolution was analyzed, and the coating thickness estimation was carried out using peak delays of correlation profiles taken from each coating layer.

Eight major categories of active infrared thermography NDT techniques are listed in Table 1, and a comparison of the application and characteristics of these various active infrared thermography NDT techniques is provided.

5 Conclusions

The detection principle and application status of the active infrared thermography NDT techniques in TBCs have been summarized and presented.

The optical infrared thermography testing has been widely used in surface crack defects NDT, interface disband defects NDT, and coating thickness NDT because of its simplicity, high efficiency, and easy operation. The microwave thermography testing is mainly used in interface disband defects NDT due to non-uniform heating, near-field heating, and limited heating area, therefore it is not suitable for surface crack defects NDT and coating thickness NDT. Although the ultrasonic infrared thermography testing is not directly used for TBC NDT, it is applied to composite and polymer specimens [122–126]. Besides, it is also used for testing cracks in service-retired gas turbine blades without TBC [127], which provides a theoretical and practical basis for the ultrasonic infrared thermography testing in TBC.

Considering existing research results, this technique is progressing in quantitative detection, high precision detection, automatic and fast detection, and adaptability for engineering applications.

5.1 Quantitative Detection

The infrared thermography testing in TBCs is shifting from qualitative testing to quantitative testing. In the past, researchers have detected disbond defects and surface defects in TBCs by active infrared thermography NDT techniques and post-processing algorithms [65, 87, 108, 109, 113, 128]. Now, researchers have also tried to quantitatively disbond detect defects by using algorithms such as neural networks, principal component analysis, and projected infrared fringe method, although the detection accuracy still needs to be improved [107, 110]. The quantitative detection of coating thickness is also the main research topic at present, and certain breakthroughs [114–119, 121] have been made. The bond coating thickness on the turbine blade is 75 to 150 μm [5], and it will fail when the disbond coating reaches tens of microns in the actual operating environment. However, the current disbond coating used for experimental analysis is far beyond the actual [65, 97, 107–110, 113]. Besides,

Table 1 Application and characteristics of various active infrared thermography NDT techniques

Technique	Sensitivity in NDT of TBCs	Advantage	Disadvantage
Optical pulsed thermography	Coating thickness: 32.5 µm [115], disbond diameter: 1 mm [110], disbond depth: 0.5 mm [110]	Simple, fast speed and high efficiency [37–43, 115–119]	Not suitable for complex structural specimens, limited detection depth [37–43, 115–119]
Optical lock-in thermography	Coating thickness: 320 µm [24], disbond diameter: 2 mm [113], disbond depth: 0.3 mm [113]	Small thermal load, suppress noise, less sensitive to local changes in surface emissivity [24, 36, 57–62, 110, 113]	Low efficiency, over-reliance on excitation source, easy to ignore blind frequency phenomenon [24, 36, 57–62, 113, 120]
Linear scanning thermography	Surface crack width: 63 µm [65], blind hole diameter: 2 mm [95, 96], blind depth: 0.4 mm [95, 96]	Speed controllable, with spatial and temporal information [64, 65, 107, 108]	Small detection area, more processing algorithms [64, 65, 107, 108]
Point scanning thermography	Surface crack width: 9.5 µm [65], blind hole diameter: 1 mm [107, 108], blind hole depth: 1.9 mm [107, 108]	High sensitivity, speed controllable, with spatial and temporal information, quantification [65, 71, 72]	low efficiency, small detection area, more processing algorithms [65, 71, 72]
Grating scanning thermography	Lack of experimental verification [36, 73]	Simultaneous detection of Horizontal and vertical crack, localizable detection, low requirement for sampling frequency [36, 73]	Lack of experimental verification, no satisfactory heat sources [36, 63]
Non-stationary thermal wave imaging testing	Coating thickness: 320 µm [75]	Flexibility, high sensitivity, safe operation[75]	Lack of experimental verification [75]
Ultrasonic infrared thermography	Lack of experimental verification [36]	Strong penetration, high detection depth, high sensitivity, safe operation, quantification [28, 36, 80–87]	High requirement for surface finish of specimens, high requirement for couplant filled in specimens [28, 36, 80–87]
Eddy current thermography	Blind hole diameter: 50 µm [97], blind hole diameter: 2 mm [97]	Low-cost, inner heating, high resolution, great sensitivity, quantification [94–100]	Limited to conductive material, non-uniform heating, near-field heating, limited heating area [94–100]
Dielectric loss thermography	Not suitable for NDT of TBCs [90]	Full-field, high resolution, high sensitivity, quantification, uniform heating, selective heating [90–93]	Not suitable for NDT of TBCs, non-uniform heating, complex heating system, electromagnetic radiation [90–93]

quantitative detection of the diameter-depth ratio and aspect-ratio of disbond defects is also crucial for the performance detection of TBC. Therefore, the quantitative detection of the three-dimensional information of the disbond coating is an inevitable development trend.

5.2 High Precision Detection

The quantitative detection of defects in TBCs is a necessary development trend, but the detection accuracy is not completely satisfactory. Therefore, high precision detection has become an inevitable demand. When researchers use the projected infrared fringe method to exactly locate disbond defects, the relative error range between the reconstructed measured value and the true height value is 2.76%-4.23%

[107]. However, the disbond defects in literature [107] are regular. In the actual defect detection, the accuracy of this method has yet to be verified. Quantitative detection of disbond defects' diameter and depth has been carried out using optical pulsed thermography testing technique and Markov-PCA-BP algorithm [110]. The depth and diameter prediction error is about 4% ~ 10%, which proved the defect detection accuracy still needs to be improved. In recent years, the research on coating thickness in TBCs has undergone a process of qualitative analysis and quantitative detection, and the detection accuracy under different algorithms has been increased from 89 to 95% [114–121]. Therefore, high precision detection of coating thickness is also a future trend.

5.3 Automatic and Fast Detection

TBCs have been widely used in modern industry and it plays an important role, therefore, automatic and real-time detection of surface crack defects, interface disbond defects, and coating thickness has great significance. With the application of deep learning algorithms such as neural networks in disbond defects detection and coating thickness detection [110, 115, 116], automatic and real-time detection has been achieved. However, many other advanced deep learning algorithms such as Fast R-CNN [129], Faster R-CNN [130], RFCN [131], ResNet-101 [132], and Mask R-CNN [133] can also be applied to these fields to further improve the automatic and fast detection ability.

5.4 Adaptability for Engineering Applications

Most of the current active infrared thermography NDT techniques and corresponding algorithms are for flat-bottomed defects [65, 97, 106, 108, 109, 113]. But in actual situations, the surface of the blade where the TBC is located in a complex non-planar structure. In a real engineering application situation, heat flows from the bottom surface to the top surface and from the edge to the center of a TBC as a result of the eddy current effect, geometric heating effect, heat conductivity, and heat diffusion. Given that the temperature distribution is extremely non-uniform, the raw thermal images collected by the infrared camera shield the information on the location and shape of the weak disbond defect. Thus, the non-uniform or uneven temperature distribution should be eliminated to highlight the defect information.

Due to the complexity of the actual service conditions and the limitations of the algorithm, the active infrared thermography NDT techniques have not been completely developed from laboratory research into conventional testing techniques which meet the needs of many engineering applications. Therefore, the research and development of adaptive, high signal-to-noise ratio, high robustness, and high reliability algorithms will also be the future trend in TBC NDT.

In conclusion, quantitative detection, high precision detection, automatic and fast detection, and adaptability for engineering applications are the main trend in NDT for TBCs based on infrared thermography.

References

1. Nathan, S. Jewel in the Crown: Rolls-Royce's Single-Crystal Turbine Blade Casting Foundry. August (2015)
2. Essienubong, I.A., Ikechukwu, O., Ebunilo, P.O., Ikpe, E.: Material selection for high pressure (HP) turbine blade of conventional turbojet engines. Am. J. Mech. Ind. Eng. **1**(1), 1–9 (2016)
3. Lima, R.S., Guerreiro, B.M., Aghasibeig, M.: Microstructural characterization and room-temperature erosion behavior of as-deposited SPS, EB-PVD and APS YSZ-based TBCs. J. Therm. Spray Technol. **28**(1–2), 223–232 (2019). https://doi.org/10.1007/s11666-018-0763-6
4. Bernard, B., Quet, A., Bianchi, L., Joulia, A., Malié, A., Schick, V., Rémy, B.: Thermal insulation properties of YSZ coatings: suspension plasma spraying (SPS) versus electron beam physical vapor deposition (EB-PVD) and atmospheric plasma spraying (APS). Surf. Coat. Technol. **318**, 122–128 (2017). https://doi.org/10.1016/j.surfcoat.2016.06.010
5. Padture, N., Gell, M., Jordan, E.: Thermal barrier coatings for gas-turbine engine applications. Science **296**(5566), 280–284 (2002). https://doi.org/10.1126/science.1068609
6. Schulz, U., Leyens, C., Fritscher, K.: Some recent trends in research and technology of advanced thermal barrier coatings. Aerosp. Sci. Technol. **7**(1), 73–80 (2003). https://doi.org/10.1016/S1270-9638(02)00003-2
7. Bi, X., Xu, H., Gong, S.: Investigation of the failure mechanism of thermal barrier coatings prepared by ele-ctron beam physical vapor deposition. Surf. Coat. Technol. **130**(1), 122–127 (2000). https://doi.org/10.1016/S0257-8972(00)00693-9
8. Schumann, E., Sarioglu, C., Blachere, J.R., et al.: High-temperature stress measurements during the oxidation of NiAl. Oxid. Met. **53**(3–4), 259–272 (2000). https://doi.org/10.1023/A:1004585003083
9. Yang, L., Zhou, Y.C., Lu, C.: Damage evolution and rupture time prediction in thermal barrier coatings sub-jected to cyclic heating and cooling: an acoustic emission method. Acta Mater. **59**(17), 6519–6529 (2011). https://doi.org/10.1016/j.actamat.2011.06.018
10. Yang, L., Zhou, Y.C., Mao, W.G., Liu, Q.X.: Acoustic emission evaluation of the fracture behavior of APS-TBCs subjecting to bond coating oxidation. Surf. Interface Anal. **39**(9), 761–769 (2010). https://doi.org/10.1002/sia.2586
11. Manero, A.C., Knipe, K., Meid, C., Wischek, J., Lacdao, C., Smith, M., Okasinski, J., Almer, J., Bartsch, M., Karlsson, A.: Comparison of thermal barrier coating stresses via high energy X-rays and piezospectros-copy. AIAA. 2015–0874 (2015) https://doi.org/10.2514/6.2015-0874
12. Sankar, B., Thiyagasundaram, P.: Crack opening displacement as a criterion for crack propagation in ther-mal barrier coatings. In: 47th AIAA Aerospace Sciences Meeting Including the New Horizons Forum and Aerospace Exposition, AIAA Paper 2009–1428 (2013) https://doi.org/10.2514/6.2009-1428
13. Ghasemi, R., Shoja-Razavi, R., Mozafarinia, R., Jamali, H.: The influence of laser treatment on thermal sho-ck resistance of plasma-sprayed nanostructured yttria stabilized zirconia thermal barrier coatings. Ceram. Int. **40**(1), 347–355 (2014). https://doi.org/10.1016/j.ceramint.2013.06.008
14. Zhou, B., Kokini, K.: Effect of surface pre-crack morphology on the fracture of thermal barrier coatings und-er thermal shock. Acta Mater. **52**(14), 4189–4197 (2004). https://doi.org/10.1016/j.actamat.2004.05.035
15. Avdelidis, N.P., Almond, D.P., Dobbinson, A.: Aircraft composites assessment by means of transient thermal NDT. Prog. Aerosp. Sci. **40**, 143–162 (2004). https://doi.org/10.1016/j.paerosci.2004.03.001

16. Barden, T.J., Almond, D.P., Morbidini, M.: Advances in thermosonics for detecting impact damage in CFRP composites. Insight-Non-Destr. Test. Cond. Monit. **48**, 90–93 (2006). https://doi.org/10.1784/insi.2006.48.2.90

17. Pickering, S.G., Almond, D.P.: An evaluation of the performance of an uncooled micro bolometer array in-frared camera for transient thermography NDE. Nondestr. Test. Eval. **22**, 63–70 (2007). https://doi.org/10.1080/10589750701446484

18. Jiang, H.J., Chen, L.: Research status and development trend of pulsed infrared nondestructive testing technology. Infrared Technol. **40**, 946–951 (2007)

19. Ptaszek, G., Cawley, P., Almond, D.: Artificial disbonds for calibration of transient thermography inspection of thermal barrier coating systems. NDT E Int. **45**, 71–78 (2012). https://doi.org/10.1016/j.ndteint.2011.09.008

20. Almond, D.P., Pickering, S.G.: An analytical study of the pulsed thermography defect detection limit. J. Appl. Phys. **093510**, 1 (2012)

21. Maldague, X.V., Marinetti, S.: Pulse phase infrared thermography. Appl. Phys. **79**, 2694–2698 (1996). https://doi.org/10.1063/1.362662

22. Vallerand, S., Maldague, X.: Defect Characterization in pulsed thermography: a statistical method compared with Kohonen and perceptron neural networks. NDT E Int. **33**, 307–315 (2000). https://doi.org/10.1016/S0963-8695(99)00056-0

23. Maldague, X.V., Galmiche, F., Ziadi, A.: Advances in pulsed phase thermography. Infrared Phys. Technol. **43**, 175–181 (2002). https://doi.org/10.1016/S1350-4495(02)00138-X

24. Zhang, J.Y., Meng, X.B., Ma, Y.C.: A new measurement method of coatings thickness based on lock-in thermography. Infrared Phys. Technol. **76**, 655–660 (2016). https://doi.org/10.1016/j.infrared.2016.04.028

25. Wellman, R.G., Nicholls, J.R.: A review of the erosion of thermal barrier coatings. J. Phys. D Appl. Phys. **40**, 293–305 (2007). https://doi.org/10.1088/0022-3727/40/16/R01

26. Torkashvand, K., Poursaeidi, E., Mohammadi, M.: Effect of TGO thickness on the thermal barrier coatings life under thermal shock and thermal cycle loading. Ceram. Int. **44**, 9283–9293 (2018). https://doi.org/10.1016/j.ceramint.2018.02.140

27. Ye, D., Wang, W., Huang, J., Lu, X., Zhou, H.: Nondestructive interface morphology characterization of th-ermal barrier coatings using terahertz time-domain spectroscopy. Coatings **9**(2), 89 (2019). https://doi.org/10.3390/coatings9020089

28. Li, Y., Yan, B., Li, W., Li, D.: Thickness assessment of thermal barrier coatings of aeroengine blades via dual-frequency eddy current evaluation. IEEE Magn. Lett. **7**, 1–5 (2016). https://doi.org/10.1109/LMAG.2016.2590465

29. Ibarra-Castanedo, C., Gonzalez, D., Klein, M., Pilla, M., Vallerand, S., Maldague, X.: Infrared image proce-ssing and data analysis. Infrared Phys. Technol. **46**(1–2), 75–83 (2004). https://doi.org/10.1016/j.infrared.2004.03.011

30. Marinetti, S., Finesso, L., Marsillo, E.: Matrix factorization methods: Application to thermal NDT/E. NDT and E Int. **39**(8), 611–616 (2006). https://doi.org/10.1016/j.ndteint.2006.04.008

31. Marinetti, S., Grinzato, E., Bison, P.G., Bozzi, E., Chimenti, M., Pieri, G., Salvetti, O.: Statistical analysis of IR thermographic sequences by PCA. Infrared Phys. Technol. **46**(1–2), 85–91 (2004). https://doi.org/10.1016/j.infrared.2004.03.012

32. Busse, G., Wu, D., Karpen, W.: Thermal wave imaging with phase sensitive modulated thermography. J. Appl. Phys. **71**, 3962 (1992). https://doi.org/10.1063/1.351366

33. Wu, D., Salerno, A., Busse, G.: Lock-in thermography for nondestructive evaluation of aerospace structures. In: Proceedings of the 7th European Conference on Non-Destructive Testing. 26–29 (1998)

34. Dillenz, A., Busse, G., Wu, D.: Ultrasound Lock-in thermography: Feasibilies and limitation. In: Proceed-ings of the Diagnostic Imaging Technologies and Industrial Applications. 3827, 10–15 (1999). https://doi.org/10.1117/12.361008

35. Wu, D., Busse, G.: Lock-in thermography for nondestructive evaluation of materials. Rev. Gen. Therm. **37**, 693–703 (1998). https://doi.org/10.1016/S0035-3159(98)80047-0

36. Qu, Z., Jiang, P., Zhang, W.: Development and application of infrared thermography non-destructive testing techniques. Sensors. **20**(14), 3851 (2020). https://doi.org/10.3390/s20143851

37. Hedayatrasa, S., Poelman, G., Segers, J., Van Paepegem, W., Kersemans, M.: Performance of frequency and/ or phase modulated excitation waveforms for optical infrared thermography of CFRPs through thermal wave radar: a simulation study. Compos. Struct. **225**, 111177 (2019). https://doi.org/10.1016/j.compstruct.2019.111177

38. Ciampa, F., Mahmoodi, P., Pinto, F., Meo, M.: Recent advances in active infrared thermography for non-destructive testing of aerospace components. Sensors. **18**(2), 609 (2018). https://doi.org/10.3390/s18020609

39. Antolis, C., Rajic, N.: Optical lock-in thermography for structural health monitoring–a study into infrared detector performance. Procedia Eng. **188**, 471–478 (2017). https://doi.org/10.1016/j.proeng.2017.04.510

40. Caruso, G., Paoloni, S., Orazi, N., Cicero, C., Zammit, U., Mercuri, F.: Quantitative evaluations by infrared thermography in optically semi-transparent paper-based artefacts. Measurement **143**, 258–266 (2019). https://doi.org/10.1016/j.measurement.2019.04.086

41. Pracht, M., Swiderski, W.: Analysis of the possibility of nondestructive testing to detect defects in multi-layered composites reinforced fibers by optical IR thermography. Compos. Struct. **213**, 204–208 (2019). https://doi.org/10.1016/j.compstruct.2019.01.071

42. Poelman, G., Hedayatrasa, S., Segers, J., Van Paepegem, W., Kersemans, M.: Multi-scale gapped smoothing algorithm for robust baseline-free damage detection in optical infrared thermography. NDT & E Int. (2020). https://doi.org/10.1016/j.ndteint.2020.102247

43. Martens, U., Schröder, K. U.: Monitoring multiple damage mechanisms in crack-patched structures using optical infrared thermography. Fatigue and Fracture of Engineering Materials and Structures. (2020) https://doi.org/10.22541/au.159362266.62095248

44. Derusova, D.A., Vavilov, V.P., Guo, X., Druzhinin, N.V.: Comparing the efficiency of ultrasonic infrared thermography under high-power and resonant stimulation of impact damage in a CFRP composite. Russ. J. Nondestr. Test. **54**(5), 356–362 (2018). https://doi.org/10.1134/S1061830918050030

45. Umar, M.Z., Vavilov, V., Abdullah, H., Ariffin, A.K.: Quantitative study of local heat sources by Ultrasonic Infrared Thermography: an approach for estimating total energy released by low energy impact damage in C/C composite. Composite B **165**, 167–173 (2019). https://doi.org/10.1016/j.compositesb.2018.11.124

46. Yang, Z., Kou, G., Li, Y., Zhang, W., Feng, J., Xu, Q., Zhao, Z.: Effects of contact interface roughness and sample mass on vibration characteristics in ultrasonic infrared thermography. IEEE Access. **8**, 127631–127639 (2020). https://doi.org/10.1109/ACCESS.2020.3008421

47. Foudazix, A., Mirala, A., Ghasr, M.T., Donnell, K.M.: Active microwave thermography for nondestructive evaluation of surface cracks in metal structures. IEEE Trans. Instrum. Meas. **68**(2), 576–585 (2018). https://doi.org/10.1109/TIM.2018.2843601

48. Mirala, A., Foudazi, A., Al Qaseer, M.T., Donnell, K.M.: Active microwave thermography to detect and locate water ingress. IEEE

Trans. Instrum. Meas. **69**(12), 9774–9783 (2020). https://doi.org/10.1109/TIM.2020.3003394

49. Zou, X., Mirala, A., Sneed, L.H., Al Qaseer, M.T., Donnell, K.: Detection of CFRP-concrete interfacial de-bonding using active microwave thermography. Composite Struct. (2020). https://doi.org/10.1016/j.compstruct.2020.113261

50. Mirala, A., Ghasr, M. T., Donnell, K. M.: Nondestructive assessment of microwave absorbing structures via active microwave thermography. In: 2018 IEEE International Instrumentation and Measurement Technology Conference (I2MTC) 1–6, (2018) IEEE. https://doi.org/10.1109/I2MTC.2018.8409631

51. Mirala, A., Foudazi, A., Ghasr, M.T., Donnell, K.M.: Detection of flat-bottom holes in conductive composites using active microwave thermography. J. Nondestruct. Eval. (2018). https://doi.org/10.1115/1.4040673

52. Grubbs, G.S., II., Mirala, A., Bischof, D., Ghasr, M.T., Donnell, K.M.: Measurement of the molecular dipole moment using active microwave thermography (AMT). J. Chem. Thermodyn. **151**, 106245 (2020). https://doi.org/10.1016/j.jct.2020.106245

53. Mirala, A., Zou, X., Ghasr, M. T., Sneed, L., Donnell, K. M.: Active Microwave Thermography: A Real-Time Monitoring Tool for CFRP-Concrete Bond Testing. In: 2019 IEEE International Instrumentation and Mea-surement Technology Conference (I2MTC) 1–6, (2019) https://doi.org/10.1109/I2MTC.2019.8827038

54. Zinovyev, S. V.: New medical technology–functional microwave thermography: experimental study. KnE Energy. (2018) https://doi.org/10.18502/ken.v3i2.1864

55. Parker, W.J., Jenkins, R.J., Butler, C.P., Abbott, G.L.: Flash method of determining thermal diffusivity, heat capacity, and thermal conductivity. J. Appl. Phys. **32**(9), 1679–1684 (1961). https://doi.org/10.1063/1.1728417

56. Liu, Z., Gao, J., Xie, H., Wallace, P.: NDT capability of digital shearography for different materials. Opt. Lasers Eng. **49**(12), 1462–1469 (2011). https://doi.org/10.1016/j.optlaseng.2011.04.006

57. Gleiter, A., Riegert, G., Zweachper, T.: Ultrasound lock-in thermography for advanced depth resolved defect selective imaging. Insight Non-Destr. Test. Cond. Monit. **5**, 272–274 (2007). https://doi.org/10.1784/insi.2007.49.5.272

58. Wallbrink, C., Wade, S.A., Jones, R.: The effect of size on the quantitative estimation of defect depth in steel structures using lock-in thermography. J. Appl. Phys. **101**, 104907 (2007). https://doi.org/10.1063/1.2732443

59. Bai, W., Wong, B.S.: Evaluation of defects in composite plates under convective environments using lock-in thermography. Meas. Sci. Technol. **12**, 142–150 (2001). https://doi.org/10.1088/0957-0233/12/2/303

60. Montanini, R.: Quantitative determination of subsurface defects in a reference specimen made of Plexiglas by means of lock-in and pulse phase infrared thermography. Infrared Phys. Tech. **53**, 363–371 (2010). https://doi.org/10.1016/j.infrared.2010.07.002

61. Feng, L., Tao, N., Xu, C.: Lock-in thermography and its application in nondestructive evaluation. Infrared Laser Eng. **39**, 1121–1123 (2010)

62. Denis, A., Vasyl, R.: A digital lock-in technique for small signal detection with square wave reference over a wide frequency range. In: Proceedings of the 14th International Conference on Advanced Trends in Radio elecrtronics, Telecommunications and Computer Engineering. 20–24 (2018)

63. Honner, M., Honnerová, P., Kučera, M.: Laser scanning heating method for high-temperature spectral emiss-ivity analyses. Appl. Therm. Eng. **94**, 76–81 (2016). https://doi.org/10.1016/j.applthermaleng.2015.10.121

64. Zhao, S.B., Zhang, C.L., Wu, N.M., Wang, H.M.: Quality evaluation for air plasma spray thermal barrier coatings with pulsed thermography. Prog. Nat. Sci. Mater. Int. **21**(4), 301–306 (2011). https://doi.org/10.1016/S1002-0071(12)60061-6

65. Jiao, D., Shi, W., Liu, Z., Xie, H.: Laser multi-mode scanning thermography method for fast inspection of micro-cracks in TBCs surface. J. Nondestr. Eval. **37**(2), 30 (2018). https://doi.org/10.1007/s10921-018-0485-1

66. Gruss, C., F. Lepoutre, D. Balageas.: Nondestructive evaluation using a flying-spot camera. ONERA TP (1993).

67. Gru, C.: Theoretical and experimental applications of the flying spot camera. (1992).

68. Rodríguez-Aseguinolaza, J., Colom, M., González, J., Mendioroz, A., Salazar, A.: Quantifying the width and angle of inclined cracks using laser-spot lock-in thermography. NDT and E Int. **122**, 102494 (2021). https://doi.org/10.1016/j.ndteint.2021.102494

69. Colom, M., Rodríguez-Aseguinolaza, J., Mendioroz, A., Salazar, A.: Sizing the depth and width of narrow cracks in real parts by laser-spot lock-in thermography. Materials **14**(19), 5644 (2021)

70. Bodnar, J.L., Egée, M.: Wear Crack characterization by photothermal radiometry. Wear **196**(1–2), 54–59 (1996). https://doi.org/10.1016/0043-1648(95)06837-6

71. Burrows, S.E., Dixon, S., Pickering, S.G., Li, T., Almond, D.P.: Thermographic detection of surface brea-king defects using a scanning laser source. NDT and E Int. **44**(7), 589–596 (2011). https://doi.org/10.1016/j.ndteint.2011.06.001

72. Li, T., Almond, D.P., Rees, D.A.S.: Crack imaging by scanning pulsed laser spot thermography. NDT and E Int. **44**(2), 216–225 (2011). https://doi.org/10.1016/j.ndteint.2010.08.006

73. Ibarra-Castanedo, C., Maldague, X. P.: Pulsed phase thermography inversion procedure using normalized parameters to account for defect size variations. In:Thermosense XXVII. International Society for Optics and Photonics. 5782, 334–341 (2005) https://doi.org/10.1117/12.596602

74. Qu, Z., Zhang, W., Lv, Z., Wang, F.: A new grating thermography for nondestructive detection of cracks in coatings: fundamental principle. Coatings **9**(7), 411 (2019). https://doi.org/10.3390/coatings9070411

75. Subhani, S.K., Suresh, B., Ghali, V.S.: Empirical mode decomposition approach for defect detection in non-stationary thermal wave imaging. NDT & E Int. **81**, 39–45 (2016). https://doi.org/10.1016/j.ndteint.2016.03.004

76. Vesala, G. T., Chandra Sekhar Yadav, G. V. P., Ghali, V. S., Suresh, B., and Naik, R. B. Proper Orthogonal Decomposition-Based Coating Thickness Estimation in Quadratic Frequency Modulated Thermal Wave Imaging. Advances in Non-destructive Evaluation. 51–61 (2021).

77. Mulaveesala, R., Tuli, S.: Theory of frequency modulated thermal wave imaging for nondestructive subsurface defect detection. Appl Phys Lett. **89**(19), 191913 (2006). https://doi.org/10.1063/1.2382738

78. Mulaveesala, R., Tuli, S.: Phase sensitive digitized frequency modulated thermal wave imaging and pulse compression for NDE applications. Thermosense XXVIII. Vol. 6205. International Society for Optics and Photonics. 6205: 620515 (2006).

79. Favro, L. D., Han, X., Ouyang, Z., Sun, G., Sui, H., Thomas, R. L.: IR imaging of cracks excited by an ultrasonic pulse. In: Thermosense XXII. International Society for Optics and Photonics. 4020, 182–185 (2000) https://doi.org/10.1117/12.381549

80. Vavilov, V.P., Chulkov, A.O., Derusova, D.A.: IR thermographic characterization of low energy impact damage in carbon/carbon composite by applying optical and ultrasonic stimulation. Proc. SPIE. **9105**, 91050J (2014). https://doi.org/10.1117/12.2049810

81. Han, X., Li, W., Zeng, Z., Favro, L.D., Thomas, R.L.: Acoustic chaos and sonic infrared imaging. Appl. Phys. Lett. **81**, 3188–3190 (2002). https://doi.org/10.1063/1.1516240

82. Shepard, S.M., Ahmed, T., Lhota, J.: Experimental considerations in vibro thermography. Proc. SPIE. **5405**, 332–335 (2004). https://doi.org/10.1117/12.546599

83. Krapez, J.C., Taillade, F., Balageas, D.: Untrasound-lock-in-thermography NDE of composite plates with low power actuators. Experimental investigation of the influence of the lamb wave frequency. Quant. Infrared Thermogr. **2**, 191–206 (2005). https://doi.org/10.3166/qirt.2.191-206

84. Zweschper, T., Gleiter, A., Riegert, G.: Ultrasound excited thermography using frequency modulated elastic waves. Insight Non-Destr. Test. Cond. Monit. **45**, 178–182 (2003). https://doi.org/10.1784/insi.45.3.178.53162

85. Ibarra-Castanedo, C., Piau, J.M., Guilbert, S.: Comparative study of active thermography techniques for the nondestructive evaluation of honeycomb structures. Res. Nondestruct. Eval. **20**, 1–31 (2009). https://doi.org/10.1080/09349840802366617

86. Umar, M.Z., Vavilov, V., Abdullah, H., Ariffin, A.K.: Ultrasonic infrared thermography in non-destructive testing: a review. Russ. J. Nondestr. Test. **52**(4), 212–219 (2016). https://doi.org/10.1134/S1061830916040082

87. Qu, Z., Zhang, W.X., Lv, Z.C.: A new grating thermography for nondestructive detection of cracks in coatings: fundamental principle. Coatings **9**, 411 (2019). https://doi.org/10.3390/coatings9070411

88. Liu, J., Yang, W., Dai, J.: Research on thermal wave processing of lock-in thermography based on analyzing image sequences for NDT. Infrared Phys. Technol. **53**, 348–357 (2010). https://doi.org/10.1016/j.infrared.2010.06.002

89. Osiander, R., Spicer, J.W.: Time-resolved infrared radiometry with step heating. A review. Rev. Gén. Therm. **37**, 680–692 (1998). https://doi.org/10.1016/S0035-3159(98)80046-9

90. Zhang, H., Yang, R., He, Y., Foudazi, A., Cheng, L., Tian, G.: A review of microwave thermography nondestructive testing and evaluation. Sensors **17**(5), 1123 (2017). https://doi.org/10.3390/s17051123

91. He, Y., Yang, R., Zhang, H., Zhou, D., Wang, G.: Volume or inside heating thermography using electromagn-ettic excitation for advanced composite materials. Int. J. Thermal Sci. **111**, 41–49 (2017). https://doi.org/10.1016/j.ijthermalsci.2016.08.007

92. Yang, R., He, Y.: Optically and non-optically excited thermography for composites: a review. Infrared. Phys. Technol. **75**, 26–50 (2016). https://doi.org/10.1016/j.infrared.2015.12.026

93. Meredith, R.: Engineers' Handbook of Industrial Microwave Heating. Power Eng. **13**, 3 (1999). https://doi.org/10.1049/PBPO025E

94. He, Y., Tian, G., Pan, M., Chen, D.: Impact evaluation in carbon fiber reinforced plastic (CFRP) laminates using eddy current pulsed thermography. Compos. Struct. **109**, 1–7 (2013). https://doi.org/10.1016/j.compstruct.2013.10.049

95. Pan, M., He, Y., Tian, G., Chen, D., Luo, F.: Defect characterisation using pulsed eddy current thermography under transmission mode and NDT applications. NDT & E Int. **52**, 28–36 (2012). https://doi.org/10.1016/j.ndteint.2012.08.007

96. He, Y., Yang, R.: Eddy current volume heating thermography and phase analysis for imaging characterization of interface delamination in CFRP. IEEE Trans. Ind. Inf. **11**(6), 1287–1297 (2015). https://doi.org/10.1109/TII.2015.2479856

97. Zhu, W., Liu, Z., Jiao, D., Xie, H.: Eddy current thermography with adaptive carrier algorithm for non-destructive testing of debonding defects in thermal barrier coatings. J. Nondestr. Eval. **37**(2), 31 (2018). https://doi.org/10.1007/s10921-018-0483-3

98. Tashan, J., Al-Mahaidi, R.: Investigation of the parameters that influence the accuracy of bond defect detection in CFRP bonded specimens using IR thermography. Compos. Struct. **94**(2), 519–531 (2012). https://doi.org/10.1016/j.compstruct.2011.08.017

99. Yin, A., Gao, B., Tian, G.Y., Woo, W.L., Li, K.: Physical interpretation and separation of eddy current pulsed thermography. J. Appl. Phys. **113**, 064101 (2013). https://doi.org/10.1063/1.4790866

100. Tian, G.Y., Gao, Y., Li, K., Wang, Y., Gao, B., He, Y.: Eddy current pulsed thermography with different excitation configurations for metallic material and defect characterization. Sensors. **16**(6), 843 (2016). https://doi.org/10.3390/s16060843

101. Zhou, B., Kokini, K.: Effect of preexisting surface cracks on the interfacial thermal fracture of thermal barri-er coatings: an experimental study. Surf. Coat. Technol. **187**(1), 17–25 (2004). https://doi.org/10.1016/j.surfcoat.2004.01.028

102. Sumner, I., Ruckle, D.: Development of improved-durability plasma sprayed ceramic coatings for gas turbine engines. In: 16th Joint Propulsion Conference. 1193 (1980) https://doi.org/10.2514/6.1980-1193

103. Taylor, T.A., Appleby, D.L., Weatherill, A.E., Griffiths, J.: Plasma-sprayed yttria-stabilized zirconia coat-ings: structure-property relationships. Surf. Coat. Technol. **43**, 470–480 (1990). https://doi.org/10.1016/0257-8972(90)90098-W

104. Zhong, M.L., Liu, W.: Comparative Research on Cracking Tendency in Powder Feeding Laser Cladding Stellite and NiCrSiB Alloys. Chin. J. Lasers **29**(11), 1031–1036 (2002)

105. Théry, P.Y., Poulain, M., Dupeux, M., Braccini, M.: Adhesion energy of a YPSZ EB-PVD layer in two ther-mal barrier coating systems. Surf. Coat. Technol. **202**(4–7), 648–652 (2007). https://doi.org/10.1016/j.surfcoat.2007.06.014

106. Cernuschi, F., Capelli, S., Bison, P., Marinetti, S., Lorenzoni, L., Campagnoli, E., Giolli, C.: Non-destructive thermographic monitoring of crack evolution of thermal barrier coating coupons during cyclic oxidation aging. Acta Mater. **59**(16), 6351–6361 (2011). https://doi.org/10.1016/j.actamat.2011.06.045

107. Jiao, D.C., Liu, Z.W., Zhu, W.Y., Xie, H.M.: Exact localization of debonding defects in thermal barrier coatings. AIAA J. **56**(9), 3691–3700 (2018). https://doi.org/10.2514/1.J056806

108. Liu, Z., Jiao, D., Shi, W., Xie, H.: Linear laser fast scanning thermography NDT for artificial disbond defects in thermal barrier coatings. Opt. Express **25**(25), 31789–31800 (2017). https://doi.org/10.1364/OE.25.031789

109. Ptaszek, G., Cawley, P., Almond, D., Pickering, S.: Transient thermography testing of unpainted thermal ba-rrier coating (tbc) systems. NDT&E Int. **59**, 48–56 (2013). https://doi.org/10.1016/j.ndteint.2013.05.001

110. Tang, Q., Dai, J., Liu, J., Liu, C., Liu, Y., Ren, C.: Quantitative detection of defects based on Markov–PCA–BP algorithm using pulsed infrared thermography technology. Infrared Phys. Technol. **77**, 144–148 (2016). https://doi.org/10.1016/j.infrared.2016.05.027

111. Tang, Q., Gao, S., Liu, Y., Lu, Y., Xu, P.: Experimental research on YSZ TBC structure debonding defect detection using long-pulsed excitation of infrared thermal wave non-destructive testing. Thermal Sci. **23**(3 Part A), 1313–1321 (2019). https://doi.org/10.2298/TSCI180513128T

112. Bu, C., Sun, Z., Tang, Q., Liu, Y., Mei, C.: Thermography sequence processing and defect edge identification of TBC structure debonding defects detection using long-pulsed thermal wave non-destructive testing technology. Russ. J. Nondestr. Test. **55**(1), 80–87 (2019). https://doi.org/10.1134/S1061830919010030

113. Tang, Q., Dai, J., Bu, C., Qi, L., Li, D.: Experimental study on debonding defects detection in thermal barrier coating structure using infrared lock-in thermographic technique. Appl. Therm. Eng. **107**, 463–468 (2016). https://doi.org/10.1016/j.applthermaleng.2016.07.008

114. Marinetti, S., Robba, D., Cernuschi, F., Bison, P.G., Grinzato, E.: Thermographic inspection of TBC coated gas turbine blades: Discrimination between coating over-thicknesses and adhesion

defects. Infrared Phys. Technol. **49**(3), 281–285 (2007). https://doi.org/10.1016/j.infrared.2006.06.018

115. Unnikrishnakurup, S., Dash, J., Ray, S., Pesala, B., Balasubramaniam, K.: Nondestructive evaluation of thermal barrier coating thickness degradation using pulsed IR thermography and THz-TDS measurements: a comparative study. NDT and E Int. **116**, 102367 (2020). https://doi.org/10.1016/j.ndteint.2020.102367

116. Halloua, H., Elhassnaoui, A., Saifi, A., Elamiri, A., Obbadi, A., Errami, Y.: Neural networks and genetic algorithms for the evaluation of coatings thicknesses in thermal barriers by infrared thermography data. Procedia Struct. Integr. **5**, 997–1004 (2017). https://doi.org/10.1016/j.prostr.2017.07.153

117. Tang, Q., Liu, J., Dai, J., Yu, Z.: Theoretical and experimental study on thermal barrier coating (TBC) uneven thickness detection using pulsed infrared thermography technology. Appl. Therm. Eng. **114**, 770–775 (2017). https://doi.org/10.1016/j.applthermaleng.2016.12.032

118. Bison, P. G., Marinetti, S., Grinzato, E. G., Vavilov, V. P., Cernuschi, F., Robba, D.: Inspecting thermal barrier coatings by IR thermography. In Thermosense XXV. International Society for Optics and Photonics. 5073, 318–327 (2003) https://doi.org/10.1117/12.486019

119. Shepard, S. M., Hou, Y. L., Lhota, J. R., Wang, D., Ahmed, T.: Thermographic measurement of thermal barrier coating thickness. In Thermosense XXVII. International Society for Optics and Photonics. 5782, 407–410 (2005) https://doi.org/10.1117/12.606124

120. Shrestha, R., Kim, W.: Evaluation of coating thickness by thermal wave imaging: a comparative study of pulsed and lock-in infrared thermography—Part I: simulation. Infrared Phys. Technol. **83**, 124–131 (2017). https://doi.org/10.1016/j.infrared.2017.04.016

121. Muzika, L., Švantner, M.: Flash pulse phase thermography for a paint thickness determination. In: IOP Conference Series: Materials Science and Engineering. 723, 012021 (2020). https://doi.org/10.1088/1757-899X/723/1/012021

122. Rantala, J., Wu, D., Salerno, A., Busse, G.: Lock-in thermography with mechanical loss angle heating at ultrasonic frequencies. Proc. Conf. Quant. Infrared Thermogr. **50**, 388–393 (1997)

123. Favro, L.D., Han, X., Ouyang, Z., Sun, G., Sui, H., Thomas, R.L.: Infrared imaging of defects heated by a sonic pulse. Rev. Sci. Instrum. **71**, 2418–2421 (2000). https://doi.org/10.1063/1.1150630

124. Han, X., Zeng, Z., Li, W., Islam, S., Lu, J., Loggins, V., Yitamben, E., Favro, L.D., Newaz, G., Thomas, R.L.: Acoustic chaos for enhanced detectability of cracks by sonic infrared imaging. J. Appl. Phys. **95**(7), 3792–3797 (2004). https://doi.org/10.1063/1.1652243

125. Zalameda, J.N., Winfree, W.P., Yost, W.T.: Air coupled acoustic thermography (ACAT) inspection technique. AIP Conf. Proc. **975**, 467–474 (2008). https://doi.org/10.1063/1.2902697

126. Almond, D.P., Weekes, B., Li, T., Pickering, S.G., Kostson, E., Wilson, J., Tian, G.Y., Dixon, S., Burrows, S.: Thermographic techniques for the detection of cracks in metallic components. Insight **53**(11), 614–620 (2011). https://doi.org/10.1784/insi.2011.53.11.614

127. Guo, Y., Ruhge, F.R.: Comparison of detection capability for acoustic thermography, visual inspection and Fluorescent penetrant inspection on gas turbine components. In:AIP Conference Proceedings. American Institute of Physics. 28, 1848–1854, (2009).

128. Jiao, D., Liu, Z., Shi, W., Xie, H.: Temperature fringe method with phase-shift for the 3D shape measurement. Opt. Lasers Eng. **112**, 93–102 (2019). https://doi.org/10.1016/j.optlaseng.2018.09.010

129. Girshick, R.: Fast r-cnn. In: Proceedings of the IEEE international conference on computer vision. 1440–1448 (2015) https://doi.org/10.1109/ICCV.2015.169

130. Ren, S., He, K., Girshick, R., Sun, J.: Faster r-cnn: Towards real-time object detection with region proposal networks. IEEE Trans. Pattern Anal. Mach. Intell. **39**(6), 1137–1149 (2017). https://doi.org/10.1109/TPAMI.2016.2577031

131. Dai, J., Li, Y., He, K., Sun, J.: R-fcn: Object detection via region-based fully convolutional networks. Advances in Neural Information Processing Systems. 379–387 (2016)

132. He, K., Zhang, X., Ren, S., Sun, J.: Deep residual learning for image recognition. In: Proceedings of the IEEE conference on computer vision and pattern recognition. 770–778 (2016) https://doi.org/10.1109/CVPR.2016.90

133. He, K., Gkioxari, G., Dollár, P., Girshick, R.: Mask r-cnn. In: Proceedings of the IEEE International Conference on Computer Vision. 2961–2969 (2017). https://doi.org/10.1109/ICCV.2017.322